Intermetallics 174 (2024) 108453

Contents lists available at ScienceDirect

Intermetallics

journal homepage: www.elsevier.com/locate/intermet

Influence of Cu and Si on the microstructure and properties of $CoCrFeNiCu_{1-x}Si_x$ alloys

Xuehui Hao [*], Shihao Fan, Ping Lu, Shuai Yao, Yunhao Li, Tianyan Lu, Meijie Wang, Jingru Chen, Changzheng Wang [**]

School of Materials Science and Engineering, Liaocheng University, Liaocheng, 252059, China

ARTICLE INFO

Keywords:
High entropy alloys
Cu
Si
Microstructure
Properties

ABSTRACT

The effect of Cu and Si on the microstructure and properties of $CoCrFeNiCu_{1-x}Si_x$ alloys ($x = 0$, 0.2, 0.5, 0.8 and 1) was studied in this work. The results indicate that as the x value increased from 0 to 1, the phase compositions of $CoCrFeNiCu_{1-x}Si_x$ alloys evolved from FCC + Cu-rich phases to FCC + Cu-rich + NiSi-rich phases to FCC + BCC + NiSi-rich phases. Therefore, the decrease in Cu content led to the decreasing Cu-rich phase content, whereas Si addition not only favored the formation of intermetallic compounds, but also promoted the phase transition from FCC to BCC. Due to the competition between BCC phase suppressing corrosion and Cu-rich + NiSi-rich phases inducing galvanic corrosion, the corrosion resistance of $CoCrFeNiCu_{1-x}Si_x$ alloys improved with the increasing x value. The microstructure change also resulted in an improvement in hardness and wear resistance, and a deterioration in fracture toughness of $CoCrFeNiCu_{1-x}Si_x$ alloys. Moreover, the main wear mechanism evolved from adhesive wear and abrasive wear to slight abrasive wear. Comparison among five alloys indicates that $Cu_{0.2}Si_{0.8}$ alloy exhibited the excellent comprehensive properties, revealed by the corrosion current density of 4.81×10^{-8} A/cm^2, the hardness value of 510.5 HV, the fracture toughness of 8.57 MPa·m$^{1/2}$ and the wear rate of 0.88 mm^3·N^{-1} · m^{-1}.

1. Introduction

As a new type of alloy system, high entropy alloys (HEAs) have received much attention in recent years [1–4]. Compared with traditional alloys, HEAs consist of five or more alloy elements with fractions ranging from 5 to 35 at. %, resulting in four core effects: high entropy effect, severe lattice distortion effect, sluggish diffusion effect and cocktail effect. Therefore, HEAs exhibit the unique microstructure and excellent comprehensive properties, thus demonstrating high practical value, great research value and broad development prospect. Among the reported HEAs, CoCrFeNi high entropy alloy is generally considered as an alloy base due to its single face-centered cubic (FCC) structure, excellent mechanical properties, corrosion behaviors and wear properties [5–7]. Many researchers have found that the phase composition and microstructure of CoCrFeNi base alloys can be altered by adding alloying elements, thereby affecting its properties [8–11].

Metallic Cu element that has large positive mixing enthalpy and weak bonds with other metallic elements, can be used as a promising element for improving the strength and ductility of HEAs. For example, Miao et al. [12] have reported that the tensile strength, yield strength and hardness of $Cu_xCoCrFeNi$ HEAs initially increased and then increased, while the elongation and plasticity consistently increased, which was related to the change in dislocation density caused by Cu addition. Wang et al. [13] have also confirmed that both the yield strength and ultimate strength of the Cu-containing $CrFeCoNiCu_x$ alloys were higher than those of the Cu-free alloy. However, the results obtained by Meng et al. [14,15] show that the precipitation of Cu-rich phase could weaken the solid solution strengthening effect and thus deteriorate the surface hardness and wear resistance of CoCrFeNiCu coatings. Muangtong et al. [16] have found that Cu-rich phase at grain boundaries would be severely corroded, leading to the deterioration of the corrosion properties of CoCrFeNi alloys. Cai et al. [17] have reported that Cu element could reduce the high-temperature oxidation resistance of $FeCoCrNiCu_x$ cladding layers due to the formation of the large oxides. These results show that Cu addition is detrimental to the hardness, wear resistance and corrosion resistance of HEAs. Therefore, the chemical

---

[*] Corresponding author.

[**] Corresponding author.

E-mail addresses: janlearn@126.com (X. Hao), wangchangzheng@lcu.edu.cn (C. Wang).

https://doi.org/10.1016/j.intermet.2024.108453
Received 23 May 2024; Received in revised form 17 July 2024; Accepted 10 August 2024

composition of HEAs needs to be further optimized to obtain the excellent comprehensive properties.

Non-metallic Si element that has a similar atomic radius and a negative enthalpy of mixing with metallic elements, has also been reported to greatly affect the microstructure and comprehensive properties of HEAs. Huang et al. [18] have found that the addition of Si in FeCoCrNi alloys caused the formation of BCC and NiSi-rich phases, resulting in the increased hardness and wear resistance. The results obtained by Gu et al. [19] have also confirmed that Si element could promote the formation of BCC phase, which prevented FCC phase from being corroded. The increasing BCC content and grain refinement caused by the increasing Si content improved the corrosion resistance of $Al_{0.3}CoCrFeNiSi_x$ alloys. Zhu et al. [20] have found that Si element could refine the grain size, increase the degree of work hardening and improve the wear resistance of $FeCoCrNiSi_x$ high entropy alloy coatings. Accordingly, Si element is beneficial for the hardness, corrosion resistance and wear resistance of HEAs. Therefore, it is expected to obtain CoCrFeNi HEAs with high hardness, high fracture toughness, excellent corrosion resistance and wear resistance through synergistic effects of Cu and Si. Garip [21] has reported that the improved effect of co-added Si and Cu on the oxidation performance of $Fe_2CoCrNi_{0.5}$ alloys was not as good as that of Si alone, the mechanism behind the synergistic effect of Si and Cu on the properties of HEAs needed further research.

In this work, $CoCrFeNiCu_{1-x}Si_x$ ($x = 0, 0.2, 0.5, 0.8, 1$) alloy systems were designed to study the synergistic effects of Cu and Si alloying on microstructure, hardness, fracture toughness, corrosion resistance and tribological property of CoCrFeNi HEAs. We believe that this study would help to further expand the applications of CoCrFeNi series HEAs in engineering.

2. Experimental method

2.1. Materials preparation

In this work, Co, Cr, Fe, Ni, Cu, Si powders (purity> 99.5 wt %) were used as raw materials for melting $CoCrFeNiCu_{1-x}Si_x$ ($x = 0, 0.2, 0.5, 0.8, 1$, defined as Cu_1Si_0, $Cu_{0.8}Si_{0.2}$, $Cu_{0.5}Si_{0.5}$, $Cu_{0.8}Si_{0.2}$, Cu_0Si_1 alloys, respectively) high entropy alloys. The raw powders were mixed by manual grinding and then cold-pressed into a cylinder under a uniaxial pressure of 50 MPa. Subsequently, the cylinders were placed in a water-cooled copper crucible of the DHL 300A non-consumable arc melting furnace. Next, the vacuum was reduced to 4×10^{-3} Pa and then filled with high-purity argon gas to 0.5 atm. The arc current was about 500 A, while the arc voltage was about 11–12 V. The ingots were melted at least five times to achieve the chemical homogeneity. Table 1 lists the actual chemical compositions of $CoCrFeNiCu_{1-x}Si_x$ alloys measured by energy dispersive spectroscopy (EDS).

2.2. Materials characterization

X-ray diffraction (XRD, D8Advance) with a Cu-Kα radiation (λ = 0.15418 nm) was used to analyze the phase constitution of samples. The 2θ scanning ranged from 30° to 100° and the scanning rate was 5°/min. A Zeiss light optical microscope (OM, Axio Cam MRc 5) and field emission scanning electron microscope (FE-SEM, JSM-6700 F) equipped with EDS were used to analyze the microstructure and elemental distribution of samples.

Table 1
The actual chemical compositions of $CoCrFeNiCu_{1-x}Si_x$ alloys (at. %).

Materials	Co	Cr	Fe	Ni	Cu	Si
Cu_1Si_0	20.27	19.86	19.37	20.2	20.3	–
$Cu_{0.8}Si_{0.2}$	19.81	19.88	19.86	20.03	16.74	3.68
$Cu_{0.5}Si_{0.5}$	20.24	20.18	20.55	20.36	9.88	8.79
$Cu_{0.2}Si_{0.8}$	20.25	19.98	20.25	20.23	4.08	15.21
Cu_0Si_1	20.48	19.81	20.83	20.32	–	18.56

2.3. Electrochemical measurements

The electrochemical behaviors of samples in a 3.5 wt % NaCl solution were performed by an Autolab PGSTAT302 electrochemical workstation. The three-electrode system consisted of sample as the working electrode (WE), platinum plate as the counter electrode, the saturated calomel electrode (SCE) as the reference electrode. Open circuit potential (OCP) was measured for 30 min to form a stable electrochemical system. Electrochemical impedance spectroscopy (EIS) measurements were performed in the frequency range from 10^5 to 10^{-2} Hz at a sinusoidal signal amplitude of 0.01 V. Polarization curves were performed in the range of $-0.3\ V_{vs.\ OCP} \sim 1.2\ V_{vs.\ SCE}$ with a scan rate of 30 mV/min. The corrosion potential (E_{corr}) and corrosion current (I_{corr}) were calculated by the Tafel extrapolation method.

2.4. Mechanical properties

A hardness tester (HVS-1000) was used to perform Vickers microhardness of samples. The load was 9.8 N and the loading time was 15 s. The microhardness test was done at least five times to ensure the precision and repeatability. Meanwhile, a Nano indenter tester (KLA G200) equipped with a Berkovich indenter tip was used to detect the hardness (H) and elastic modulus (E) of samples. The tests were performed by driving the indenter at a constant load mode. The maximum applied load for the indentation test was 50 mN and the loading rate was 2.5 mN/s. The indenter type was a triangular pyramid indenter with a tip angle of 115°. Six measurements were tested on each sample to ensure the data precision. The typical load versus indentation depth curve exhibited in Fig. 1 could be expressed as follows:

$$P = \begin{cases} \alpha_1 \left(\dfrac{h}{h_l}\right)^m & 0 \le h \le h_l \\ P_m\ h_l \le h \le h_m \\ \alpha_2 (h - h_r)^n\ h_r \le h \le h_m \end{cases} \tag{1}$$

where P and P_m are the applied load and peak load, respectively. h is the indentation depth under the load of P, h_l and h_r are the indentation depth under the peak load before the creeping and the residual depth after unloading, respectively. α_1, α_2, m and n are the curve constants.

The fracture toughness (K_{IC}) of samples could also be obtained by nanoindentation test and energy-based method, and the corresponding

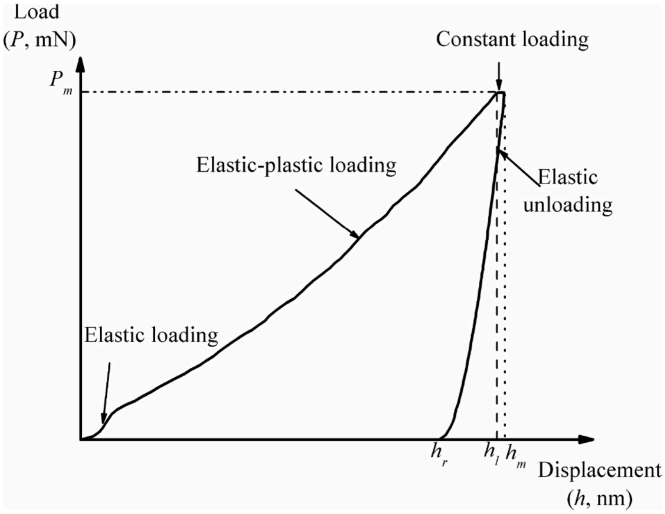

Fig. 1. A schematic illustration of a typical load versus indenter displacement (P-h) curve.

equation was as follows [22,23]:

$$K_{IC} = \sqrt{\frac{U_{fracture}}{A_m}\frac{E}{1-\nu^2}} \tag{2}$$

$$A_m = 24.56{h_m}^2 \tag{3}$$

$$U_{fracture} = \left[1 - \frac{m+1}{3} + \frac{m+1}{n+1}\frac{h_m - h_r}{h_m + m(h_m - h_l)}\right] P_m h_l \left(\frac{h_m}{h_l} - \frac{m}{m+1}\right) - P_m \frac{h_m - h_r}{n+1} \tag{4}$$

where $U_{fracture}$ is the fracture energy, A_m is the fracture area, h_m is the maximum depth after the peak load before the creeping. E is the Young's modulus of the tested samples and ν is Poisson's ratio that was reported to be about 0.3 [24,25].

2.5. Tribological properties

The reciprocating electrochemical corrosion friction and wear tester (MFT-EC4000) was used to perform the dry sliding tribological behaviors of samples at room temperature, in which the sliding distance was adjusted by modifying the eccentric distance between the connecting rod and the rotary table. The counterpart material was GCr15 steel ball with a diameter of 6 mm due to its high hardness, good wear resistance and wide application as a bearing material. Based on our previous study [10], the test parameters were set as follows: the normal load was 2 N, the scratch length was 5 mm, the sliding velocity was 0.02 m/s and the sliding time was 30 min. The morphologies and element distribution of the worn surface were observed by SEM/EDS. Meanwhile, X-ray photoelectron spectroscopy (XPS, ESCALAB 250) with an Al Ka target was used to perform the state of each element on the worn surface. The profiles of the wear track were performed by a two-dimensional optical profiler (Alpha Step IQ profile meter). Then, the wear rate (W) could be calculated using the following equation.

$$W = \frac{V}{P \bullet S} \tag{5}$$

where V is the worn volume (mm^3), P is the applied normal load (N) and S is the sliding distance (m).

3. Results and discussion

3.1. XRD analysis

Fig. 2(a, b) shows the XRD patterns of CoCrFeNiCu$_{1\text{-}x}$Si$_x$ alloys. It can be seen from Fig. 2(a) that Cu$_1$Si$_0$ alloy was composed of FCC (PDF card #65–6291) and Cu-rich (PDF card #04–0836) phases, which is consistent with the results obtained by other researchers [12,13]. This was because the mixing enthalpy between Cu and other elements was more positive, which was listed in Table 2. As the x value increased to 0.2, Cu$_{0.8}$Si$_{0.2}$ alloy still consisted of FCC and Cu-rich phases, suggesting that Si might be mainly solid solution in the FCC phase structure. However, the ratios of the peak intensity of the (111)$_{\text{Cu}}$ and (111)$_{\text{FCC}}$ shown in Fig. 2(b) were 0.54 for Cu$_1$Si$_0$ alloy and 0.33 for Cu$_{0.8}$Si$_{0.2}$ alloy, respectively, suggesting the change in phase fractions caused by the decreasing Cu content. For Cu$_{0.5}$Si$_{0.5}$ and Cu$_{0.2}$Si$_{0.8}$ alloys, the peak corresponding to NiSi-rich (PDF card #15–0793 and 32–0699) and BCC (PDF card #38–0419) phases began to appear. Finally, Cu$_0$Si$_1$ alloy was composed of BCC, FCC and NiSi-rich phases, and Cu-rich phase was not detected. These results indicate that the increasing Si content not only caused the phase transition from FCC to BCC, but also promoted the formation of intermetallic compounds.

Table 2
The mixing enthalpy (ΔH_{mix}) of different pairs atoms in CoCrFeNiCu$_{1\text{-}x}$Si$_x$ alloys (KJ•mol^{-1}).

Elements	Co	Cr	Fe	Ni	Cu	Si
Co	0	−4	−1	0	6	−38
Cr		0	−1	−7	12	−37
Fe			0	−2	13	−35
Ni				0	4	−40
Cu					0	−19
Si						0

In order to clarify the phase evolution of CoCrFeNiCu$_{1\text{-}x}$Si$_x$ alloys with the increasing x value, the phase content and lattice constants were calculated using the Rietveld refinement method and shown in Fig. 2(c and d). Fig. 2(c) shows that the volume fraction of Cu-rich phase decreased from 28.1 % to 0 %, confirming that the formation of Cu-rich phase in high entropy alloys was caused by the presence of Cu. Fig. 2(c) also indicates that as the x value increased from 0 to 0.5, the content of FCC phase continuously increased to the maximum value at $x = 0.5$. This could be explained by the fact that the change in phase fraction induced by the increasing Si content was not as prominent as that for the decreasing Cu content because Si was mainly dissolved in the FCC phase at the low x value. Meanwhile, Fig. 2(d) shows that the competitive effect between Cu that caused lattice expansion and Si that caused lattice contraction led to a slight decrease in the lattice constant [20,21]. As the x value further increased from 0.5 to 1, the content of the FCC phase continuously decreased. This might be because that Si, in addition to being solidly dissolved in the FCC phase, also promoted the formation of NiSi-rich and BCC phases. At the x value of 0.5, Si preferentially combined with other metallic elements to form intermetallic compounds, due to the more negative mixing enthalpy listed in Table 2. Therefore, NiSi-rich phase with the area fraction of 1.7 % was first detected in the Cu$_{0.5}$Si$_{0.5}$ alloy. When the x value increased to 0.8, the content of NiSi-rich phase increased to 10.0 % due to the higher Si content. Meanwhile, Si started to act as a BCC former and stabilizer and promoted the transition from FCC to BCC phase with a lower atomic packing density [26]. Therefore, BCC phase with the area fraction of 24.2 % was detected in the Cu$_{0.8}$Si$_{0.2}$ alloy. As the x value increased up to 1.0, the continuous decrease in the lattice constant as shown in Fig. 2(d) led to the fact that Si tended to promote the formation of BCC phase compared to NiSi-rich phase. Therefore, the content of NiSi-rich phase in the Cu$_0$Si$_1$ alloy decreased to 8.9 %, while that of BCC phase continuously increased to 82.8 %, which is shown in Fig. 2(c).

Fig. 2(d) also shows the calculated grain size using the (111) diffraction peak according to the Scherrer equation. It can be seen that the average grain size of the FCC phase was about 31.3 μm for Cu$_1$Si$_0$ alloy, 36.9 μm for Cu$_{0.8}$Si$_{0.2}$ alloy and 38.4 μm for Cu$_{0.5}$Si$_{0.5}$ alloy, respectively. It has been reported that the addition of Cu and Si in the FeCoCrNi HEAs could reduce the grain size [20,27]. The competitive effect between the decreasing Cu content and increasing Si content finally led to an increase in the grain size of CoCrFeNiCu$_{1\text{-}x}$Si$_x$ alloys. As the x value further increased to 1, the grain size of the FCC phase decreased while that of the BCC phase increased, which could be attributed to the phase transition caused by the increasing Si content.

In order to characterize the effect of Cu and Si on the phase evolution of CoCrFeNiCu$_{1\text{-}x}$Si$_x$ alloys, a parameter (Ω) of the melting temperature (T_m) timing the mixing entropy (ΔS_{mix}) over the mixing enthalpy (ΔH_{mix}), the difference of atomic size (δ) and valence electron concentration (VEC) of CoCrFeNiCu$_{1\text{-}x}$Si$_x$ alloys were calculated by the following equations 6–11:

$$T_m = \sum_{i=1}^{n} C_i (T_m)_i \tag{6}$$

$$\Delta S_{mix} = -R \sum_{i=1}^{n} C_i \ln C_i \tag{7}$$

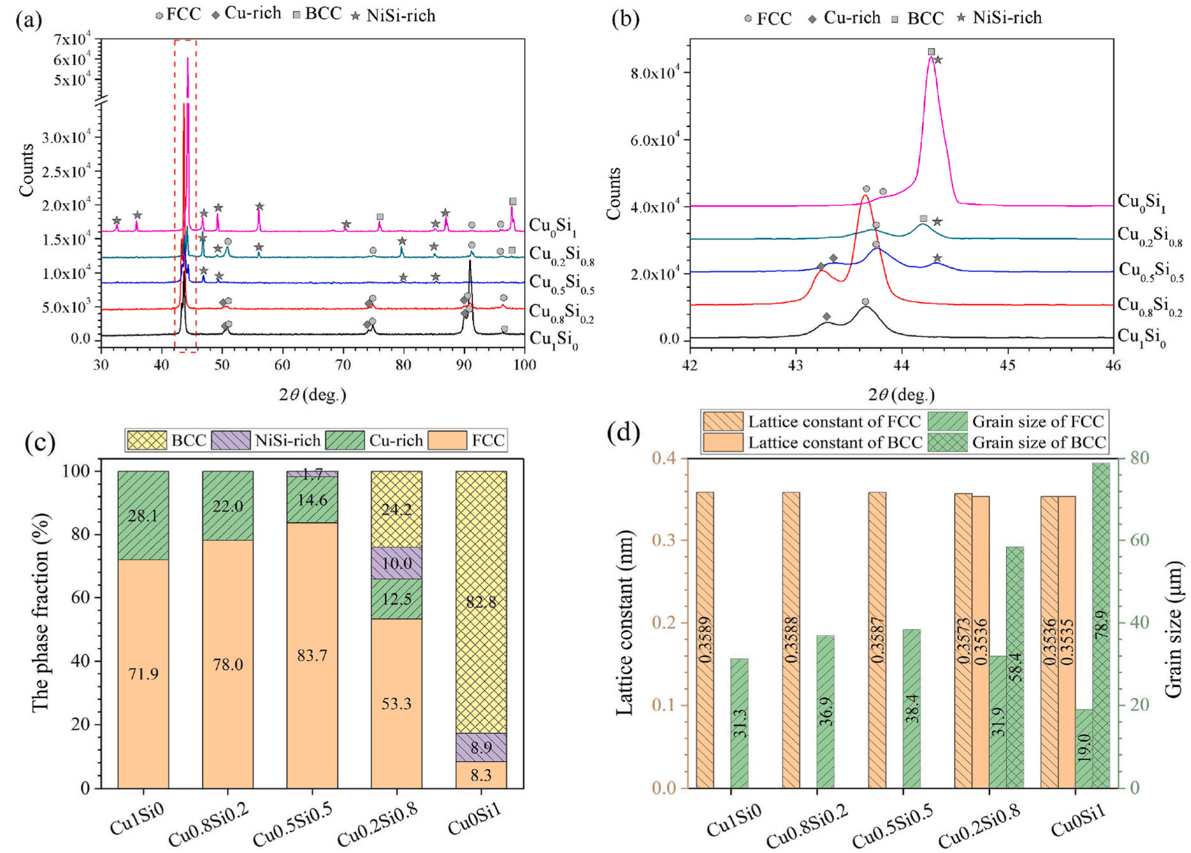

Fig. 2. XRD patterns (a) and 42°–46° magnification of (a), the phase fraction (c), the calculated lattice constant and grain size (d) of CoCrFeNi$Cu_{1-x}Si_x$ alloys.

$$\Delta H_{mix} = \sum_{i=1, i\neq j}^{n} 4\Delta H_{ij}^{mix} C_i C_j \tag{8}$$

$$\Omega = T_m \Delta S_{mix} / |\Delta H_{mix}| \tag{9}$$

$$\delta = \sqrt{\sum_{i=1}^{n} C_i \left(1 - r_i \Big/ \sum_{i=1}^{n} C_i r_i\right)^2} \tag{10}$$

$$VEC = \sum_{i=1}^{n} C_i VEC_i \tag{11}$$

where $(T_m)_i$, C_i, r_i and VEC_i represent the melting temperature, molar fraction, radius and number of valence electrons for the i_{th} element, respectively. R is the gas constant, ΔH_{ij}^{mix} is the mixing enthalpy of the binary liquid ij alloys. Tables 2 and 3 list the physicochemical and thermodynamic parameters of the constituent elements in CoCrFeNi$Cu_{1-x}Si_x$ alloys, and calculated results are listed in Table 4. Yang et al. [28] has reported that the HEAs stabilized solid-solution was located at $\Omega \geq$ 1.1 and $\delta \leq$ 6.6 %. Accordingly, five CoCrFeNi$Cu_{1-x}Si_x$ alloys were mainly composed of solid solution phases. Guo et al. [29] has reported that FCC phase was stable when *VEC* was higher than 8, while BCC phase had a value lower than 6.87. When the *VEC* value was between 6.87 and 8, BCC + FCC dual phase formed. Based on the calculated *VEC* value listed in Table 4, the phase transition from FCC to BCC was expected in CoCrFeNi$Cu_{1-x}Si_x$ alloys. Moreover, the intermetallic compound was more easily formed at a smaller Ω and a larger δ. Table 4 shows that the Ω decreased and δ increased as the x value in CoCrFeNi$Cu_{1-x}Si_x$ alloys increased. Therefore, NiSi-rich phase was detected in the $Cu_{0.5}Si_{0.5}$, $Cu_{0.2}Si_{0.8}$ and $CuSi_1$ alloys.

Table 3
The physicochemical and thermodynamic parameters of the constituent elements in CoCrFeNi$Cu_{1-x}Si_x$ alloys.

Elements	Atom radius (Å)	Pauling electronegativity	*VEC*	T_m (K)
Co	1.253	1.88	9	1768
Cr	1.249	1.66	6	2180
Fe	1.241	1.83	8	1811
Ni	1.246	1.91	10	1728
Cu	1.278	1.9	11	1358
Si	1.153	1.9	4	1687

Table 4
The calculated thermodynamic parameters of CoCrFeNi$Cu_{1-x}Si_x$ alloys.

Materials	T_m (K)	ΔS_{mix} (J•K^{-1}•mol^{-1})	ΔH_{mix} (KJ•mol^{-1})	Ω	δ (%)	*VEC*
Cu_1Si_0	1711	13.38	3.23	7.08	1.03	8.82
$Cu_{0.8}Si_{0.2}$	1732	14.18	−2.58	9.52	1.79	8.56
$Cu_{0.5}Si_{0.5}$	1776	14.45	−11.04	2.32	2.36	8.15
$Cu_{0.2}Si_{0.8}$	1810	14.21	−20.17	1.27	2.85	7.72
Cu_0Si_1	1834	13.37	−25.12	0.98	3.00	7.47

3.2. Microstructure analysis

Fig. 3 shows the SEM images and EDS mappings of CoCrFeNi$Cu_{1-x}Si_x$ alloys, whereas the EDS results of different locations in Fig. 3 are listed in Table 5. As shown in Fig. 3 (a) and (c), both Cu_1Si_0 and $Cu_{0.8}Si_{0.2}$ alloys showed a coarse dendritic structure and casting defects. The corresponding EDS mappings successively shown in Fig. 3 (b) and (d) indicate that Co, Cr, Fe and Ni elements were evenly distributed in the matrix (dark black regions), whereas Cu was enriched in grain

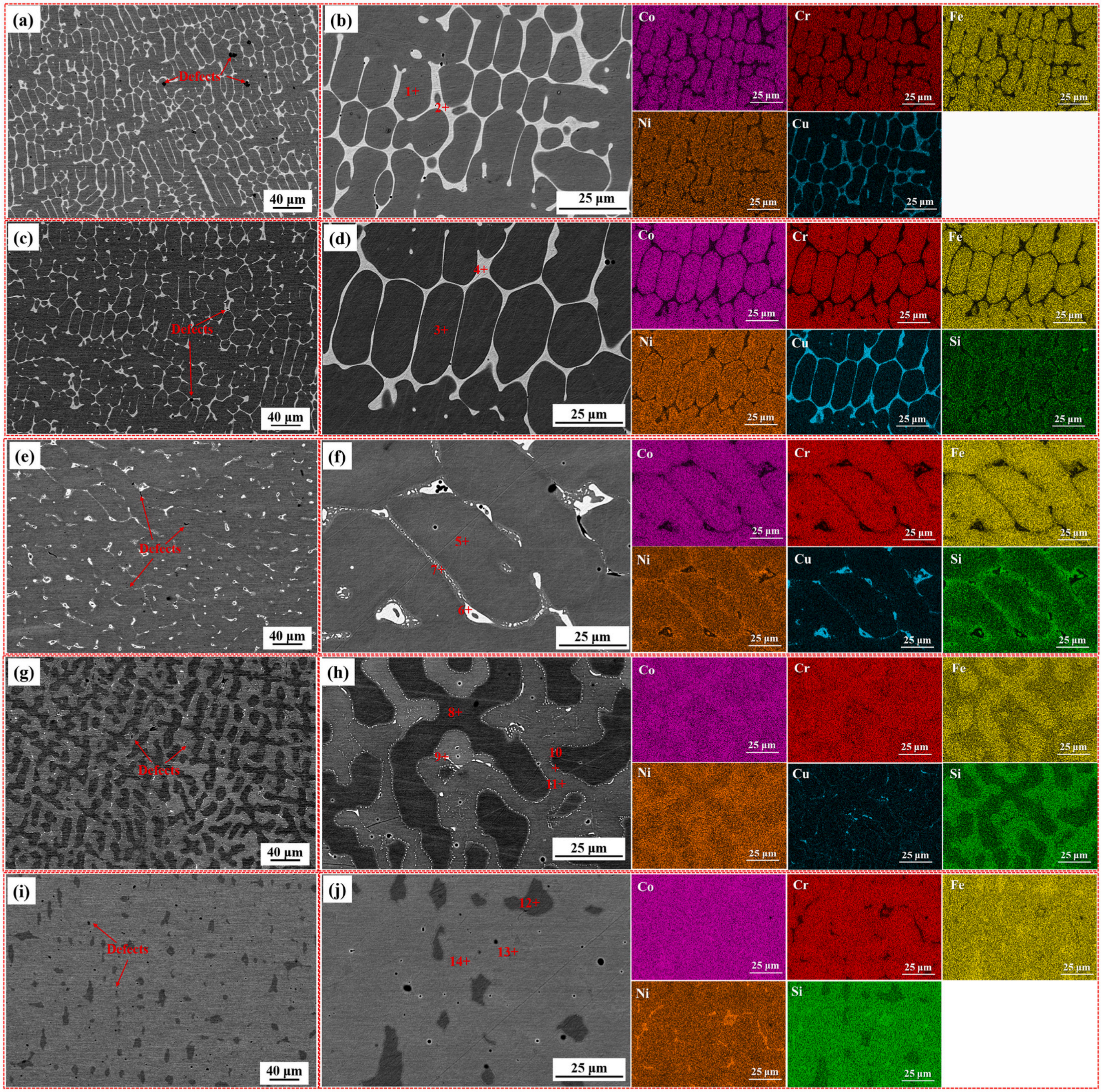

Fig. 3. SEM images and EDS results of CoCrFeNi$Cu_{1-x}Si_x$ alloys (a, b) Cu_1Si_0 alloy; (c, d) $Cu_{0.8}Si_{0.2}$ alloy; (e, f) $Cu_{0.5}Si_{0.5}$ alloy; (g, h) $Cu_{0.2}Si_{0.8}$ alloy; (I, j) Cu_0Si_1 alloy.

boundaries (bright white regions). The added Si element in the $Cu_{0.8}Si_{0.2}$ alloy was mainly solid solution in the matrix. These results are also confirmed by EDS analysis results of the matrix.

(points 1, 3) and grain boundaries (points 2, 4), which are listed in Table 5. Combined with XRD results, it can be inferred that both Cu_1Si_0 and $Cu_{0.8}Si_{0.2}$ alloys were composed of FCC matrix and Cu-rich phase segregating at grain boundaries. In Fig. 3(e), the $Cu_{0.5}Si_{0.5}$ alloy exhibited a similar microstructure to Cu_1Si_0 and $Cu_{0.8}Si_{0.2}$ alloys, but the grain boundaries became blurred. Fig. 3(f) shows that Ni and Si were rich in the grain boundaries, suggesting the formation of NiSi-rich phase. This might be because the ΔH_{mix} between Ni and Si elements was the most negative, which could promote the formation of intermetallic compounds. The high Cu content in the NiSi-rich phase (point 7 in Table 5) might be due to the chemical composition of EDS point analysis was determined from 1 μm surroundings. For the $Cu_{0.2}Si_{0.8}$ alloy, Fig. 3 (g) and (h) indicate that the Cu-rich phase still segregated at grain boundaries. Meanwhile, the matrix was divided into regions rich in Co–Cr–Fe and regions rich in Ni–Si, which could be successively assigned to FCC and BCC phases according to XRD results. NiSi-rich phase might still segregate at grain boundaries, which could be confirmed by point 10 listed in Table 5. For Cu_0Si_1 alloy, Fig. 3 (i) and (j) indicate that the Cu-rich phase completely disappeared. Meanwhile, the matrix consisted of regions rich in Co–Cr–Fe, regions evenly rich in Co–Cr–Fe–Ni–Si and regions rich in Ni–Si, which was successively confirmed by points 12, 13 and 14 listed in Table 5. Combined with XRD results, it can be inferred that Cu_0Si_1 alloy was mainly composed of FCC

Table 5
The EDS results of different locations in Fig. 3.

Materials	Points	Co	Cr	Fe	Ni	Cu	Si
Cu_1Si_0	FCC: 1	23.94	22.20	22.25	21.09	10.52	–
	Cu-rich:2	3.45	2.88	3.82	8.90	80.95	–
$Cu_{0.8}Si_{0.2}$	FCC: 3	23.62	22.18	23.16	19.33	9.12	2.59
	Cu-rich:4	3.86	3.19	3.64	8.88	79.63	0.80
$Cu_{0.5}Si_{0.5}$	FCC: 5	22.21	21.78	23.84	18.91	6.51	6.75
	Cu-rich: 6	2.92	2.01	2.84	7.93	82.32	1.98
	NiSi-rich: 7	14.09	15.10	13.54	21.93	22.01	13.33
$Cu_{0.2}Si_{0.8}$	FCC: 8	22.42	21.77	23.79	18.34	2.91	10.77
	Cu-rich: 9	4.91	4.51	4.34	7.49	75.14	4.61
	NiSi-rich: 10	15.63	16.70	15.26	18.16	19.68	14.57
	BCC: 11	19.21	19.85	17.91	21.74	2.86	18.43
Cu_0Si_1	FCC: 12	22.06	21.48	25.04	17.78	–	13.64
	NiSi-rich: 13	19.98	14.42	18.04	25.60	–	21.96
	BCC: 14	20.09	20.51	20.52	19.87	–	19.01

phase (point 12), BCC phase (point 13) and a small amount of NiSi-rich phase (point 14). Comparison of the microstructure between $Cu_{0.2}Si_{0.8}$ and Cu_0Si_1 alloys indicates that the area ratio of FCC to BCC fraction decreased with the decreasing Cu content and increasing Si content, suggesting the transformation from FCC to BCC.

3.3. Corrosion behaviors

Fig. 4 shows the potentiodynamic polarization curves of CoCrFeNi$Cu_{1\text{-}x}Si_x$ alloys in a 3.5 wt % NaCl solution. The corrosion potential (E_{corr}) and corrosion current density (I_{corr}) were obtained by Tafel extrapolation method and shown in Table 6. The E_{corr} value can represent the susceptibility of metals to gain electrons and be corroded from a thermodynamic perspective [30–32]. Therefore, the overall decrease of E_{corr} decreased with the increasing x value in CoCrFeNi$Cu_{1\text{-}x}Si_x$ alloys suggests the enhanced corrosion tendency. However, the E_{corr} cannot be used as the only parameter to evaluate the corrosion performance, the I_{corr} value that reflects an electronic flow rate can more accurately represent the corrosion resistance of metals from a dynamic perspective [30,33]. Table 6 indicates that I_{corr} decreased from 8.63×10^{-7} to 3.81×10^{-8} A/cm^2 as the x value in CoCrFeNi$Cu_{1\text{-}x}Si_x$ alloys increased from 0 to 1, suggesting a decreasing corrosion rate. Therefore, the decreasing Cu content and increasing Si content brought about an improvement in the corrosion resistance. As the potential further increased, CoCrFeNi$Cu_{1\text{-}x}Si_x$ alloys became passivated. It can be seen that Cu_1Si_0, $Cu_{0.8}Si_{0.2}$ and $Cu_{0.5}Si_{0.5}$ alloys showed a transition process from activation to passivation. Meanwhile, the transition process disappeared in $Cu_{0.2}Si_{0.8}$ and Cu_0Si_1 alloys, suggesting the spontaneous passivation process for CoCrFeNi$Cu_{1\text{-}x}Si_x$ alloys. The passive current density (I_{pass}) and pitting potential (E_{pit}) were calculated to evaluate the passivation properties of CoCrFeNi$Cu_{1\text{-}x}Si_x$ alloys and the results were listed in Table 6. Cu_0Si_1 alloy had the lowest I_{pass} and highest E_{pit}, suggesting that the protective passivation film was more easily formed on CoCrFeNi$Cu_{1\text{-}x}Si_x$ alloys with lower Cu content and higher Si content. Therefore, the decreasing Cu content and increasing Si content were beneficial for the improved corrosion self-protection ability of CoCrFeNi$Cu_{1\text{-}x}Si_x$ alloys.

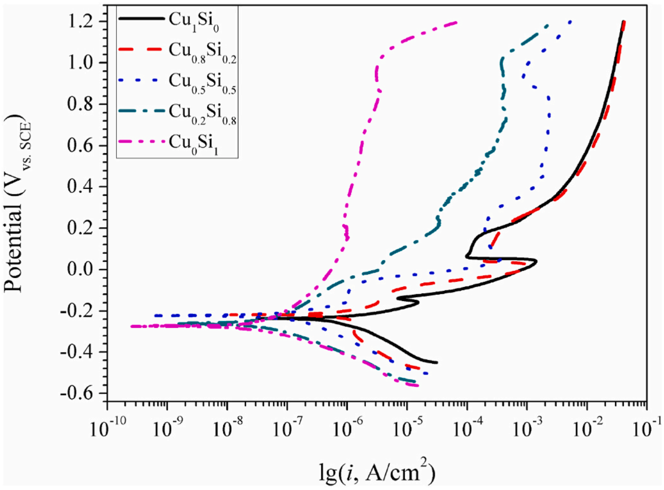

Fig. 4. Potentiodynamic polarization curves of CoCrFeNi$Cu_{1\text{-}x}Si_x$ alloys in a 3.5 wt % NaCl solution.

Table 6
The corrosion potential (E_{corr}), corrosion current density (I_{corr}), passive current density (I_{pass}) and pitting potential (E_{pit}) of CoCrFeNi$Cu_{1\text{-}x}Si_x$ alloys in a 3.5 wt % NaCl solution.

Materials	E_{corr} (V)	I_{corr} (A/cm^2)	I_{pass} (A/cm^2)	E_{pit} (V)
Cu_1Si_0	−0.236	8.63×10^{-7}	1.22×10^{-4}	0.160
$Cu_{0.8}Si_{0.2}$	−0.217	4.78×10^{-7}	2.72×10^{-4}	0.209
$Cu_{0.5}Si_{0.5}$	−0.223	1.54×10^{-7}	2.13×10^{-4}	0.268
$Cu_{0.2}Si_{0.8}$	−0.261	4.81×10^{-8}	2.04×10^{-4}	1.025
Cu_0Si_1	−0.274	3.81×10^{-8}	1.90×10^{-6}	1.067

Fig. 5 shows EIS results of CoCrFeNi$Cu_{1\text{-}x}Si_x$ alloys in a 3.5 wt % NaCl solution. In Fig. 5(a), the Bode plots of impedance modulus vs. frequency curves indicate that the impedance value at 0.01 Hz was in order of $Cu_1Si_0 < Cu_{0.8}Si_{0.2} < Cu_{0.5}Si_{0.5} < Cu_{0.2}Si_{0.8} < Cu_0Si_1$, suggesting that Cu_0Si_1 alloy had the best corrosion resistance among five alloys. The Bode plots (Fig. 5(b)) of phase angle vs. frequency curves indicate a capacitive behavior at the high frequency range that was related to the long wire or rod connecting the working electrode surface and the potentiostat [34]. Then, a wide and strong phase angle peak was observed at the medium frequency, suggesting the presence of one relaxation time constant corresponding to an electrochemical reaction. However, the surface defects and elemental segregation caused the inhomogeneous surface to be divided into areas covered with a passive film and weak areas of passive film or surface defect areas [19]. Based on the above analysis, an equivalent circuit (EC) should consist of two parts in parallel, which was shown in Fig. 5(c). In the EC, C represents the capacitance for the phase peak at the high frequency range, R_s is the electrolyte resistance, R_f and Q_f are the resistance and constant phase element (CPE) of the passive film, R_t and Q_{dl} are the charge transfer resistance and double layer capacitance. The impedance (Z_{CPE}) of CPE could be obtained by the following equation [35]:

$$Z_{CPE} = Y_0^{-1}(j\omega)^{-n} \tag{12}$$

where Y_0 represents the proportional factor, j is an imaginary number ($j^2 = -1$), ω is the angular frequency, n is the exponent of CPE ($-1 \leq n \leq 1$).

The fitting results for EIS data of CoCrFeNi$Cu_{1\text{-}x}Si_x$ alloys are listed in Table 7, which is also plotted using solid line in Fig. 5. All the fitting data had a small error range and the chi-square (χ^2) were in the order of 10^{-4}, suggesting the reliability of the fitting parameters. It can be seen that the R_f value was ranked as $Cu_1Si_0 < Cu_{0.8}Si_{0.2} < Cu_{0.5}Si_{0.5} < Cu_{0.2}Si_{0.8} < Cu_0Si_1$, which is consistent with the analysis of the polarization curves. This might be because the potential difference between the surrounding matrix and Cu-rich phase accelerated the intergranular corrosion tendency and thus the oxide film could not be easily formed on the surface [24]. Meanwhile, Si addition could promote the formation of a SiO_2 protective passive layer [36]. The R_{ct} value of CoCrFeNi$Cu_{1\text{-}x}Si_x$ alloys increased from 3.66×10^3 to 6.16×10^5 Ω·cm^2 as the x value increased from 0 to 1, suggesting an improved corrosion resistance. This was related to the microstructural transformation of CoCrFeNi$Cu_{1\text{-}x}Si_x$ alloys. On the one hand, Cu in CoCrFeNi$Cu_{1\text{-}x}Si_x$ alloys mainly segregated at grain boundaries, resulting in the severe corrosion between Cu-rich phase and surrounding matrix. Therefore, the decreasing Cu content weakened the harmful effect of the dual-phase structure on corrosion resistance. On the other hand, the addition of Si promoted the formation of BCC and NiSi-rich phases. BCC phase could act as a micro-anode to

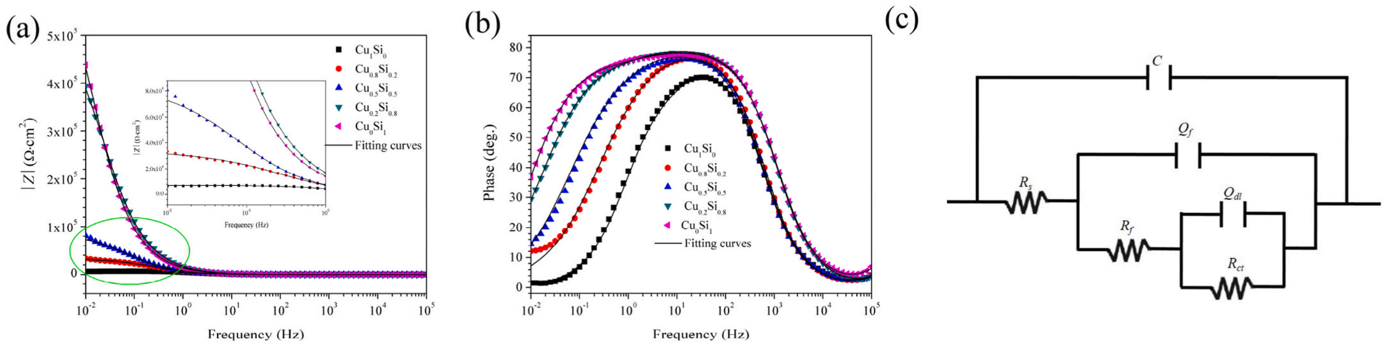

Fig. 5. EIS results (a–b) of CoCrFeNiCu$_{1\text{-}x}$Si$_x$ alloys in a 3.5 wt % NaCl solution and the equivalent circuit (c) used to fitting EIS results.

Table 7
The fitting results for EIS data corresponding to CoCrFeNiCu$_{1\text{-}x}$Si$_x$ alloys in a 3.5 wt % NaCl solution.

Materials	Cu_1Si_0	$Cu_{0.8}Si_{0.2}$	$Cu_{0.5}Si_{0.5}$	$Cu_{0.2}Si_{0.8}$	Cu_0Si_1
R_s (Ω·cm^2)	32.07 ± 5.33 %	27.98 ± 5.98 %	28.51 ± 5.78 %	33.32 ± 3.31 %	28.31 ± 3.98 %
Q_f -Y_{0f} × 10^{-5} (Ω^{-1} cm^{-2} s^n)	2.10 ± 6.63 %	2.03 ± 1.01 %	2.32 ± 1.39 %	1.05 ± 0.73 %	1.26 ± 0.64 %
n_f	0.8939 ± 6.18 %	0.905 ± 5.51 %	0.8923 ± 2.75 %	0.8989 ± 1.35 %	0.8926 ± 2.07 %
R_f × 10^4 (Ω·cm^2)	0.35 ± 4.84 %	1.05 ± 6.70 %	2.84 ± 2.78 %	6.66 ± 2.10 %	7.24 ± 1.26 %
Q_{dl}-Y_{0d} × 10^{-5} (Ω^{-1} cm^{-2} s^n)	3.12 ± 7.99 %	3.10 ± 2.31 %	2.34 ± 2.10 %	0.332 ± 4.29 %	0.330 ± 5.47 %
n_{dl}	0.7853 ± 7.55 %	0.5145 ± 6.44 %	0.5798 ± 6.95 %	0.5684 ± 4.28 %	0.6716 ± 3.67 %
R_{ct} × 10^5 (Ω·cm^2)	0.037 ± 5.18 %	0.241 ± 1.56 %	0.573 ± 1.60 %	4.98 ± 2.70 %	6.16 ± 2.94 %
Chi-squared, x^2	8.56 × 10^{-4}	7.15 × 10^{-4}	6.69 × 10^{-4}	1.16 × 10^{-4}	2.86 × 10^{-4}

prevent FCC phase as a micro-cathode from being corroded [37]. However, the formation of NiSi-rich phase led to the formation of new micro-batteries, deteriorating the corrosion resistance. The competition among above three effects finally resulted in the improvement in corrosion resistance of CoCrFeNiCu$_{1\text{-}x}$Si$_x$ alloys by the decreasing Cu content and increasing Si content.

3.4. *Mechanical properties*

Fig. 6 shows the Vickers' indentation and microhardness of CoCrFeNiCu$_{1\text{-}x}$Si$_x$ alloys. Fig. 6(a–e) indicates that a typical diamond-shaped indentation could be observed for all five alloys. However, microcracks were not detected at the ends or edges of the diamond-shaped indentation until the x value in CoCrFeNiCu$_{1\text{-}x}$Si$_x$ alloys increased to 0.8. Therefore, the fracture toughness of Cu$_{1\text{-}x}$Si$_x$ alloys might decrease with the decreasing Cu content and increasing Si content, which would be analyzed by nanoindentation test and energy-based method. Moreover, the diagonal length decreased as Cu content decreased and Si content increased. Since the hardness was inversely proportional to the square of the diagonal length [38], the microhardness of Cu$_{1\text{-}x}$Si$_x$ alloys increased from 156.7 to 890.0 HV as the x value increased from 0 to 1, which was shown in Fig. 6(f). When the x value increased from 0 to 0.2, the competitive effect between the decreasing lattice constant and increasing grain size led to a limit increase in microhardness between Cu$_1$Si$_0$ and Cu$_{0.8}$Si$_{0.2}$ alloys. As the x value further increased, the continuous decrease in the lattice constant brought about an enhanced solid-solution strengthening effect. Meanwhile, the addition of Si not only promoted the formation of hard and brittle NiSi-rich phase, but also

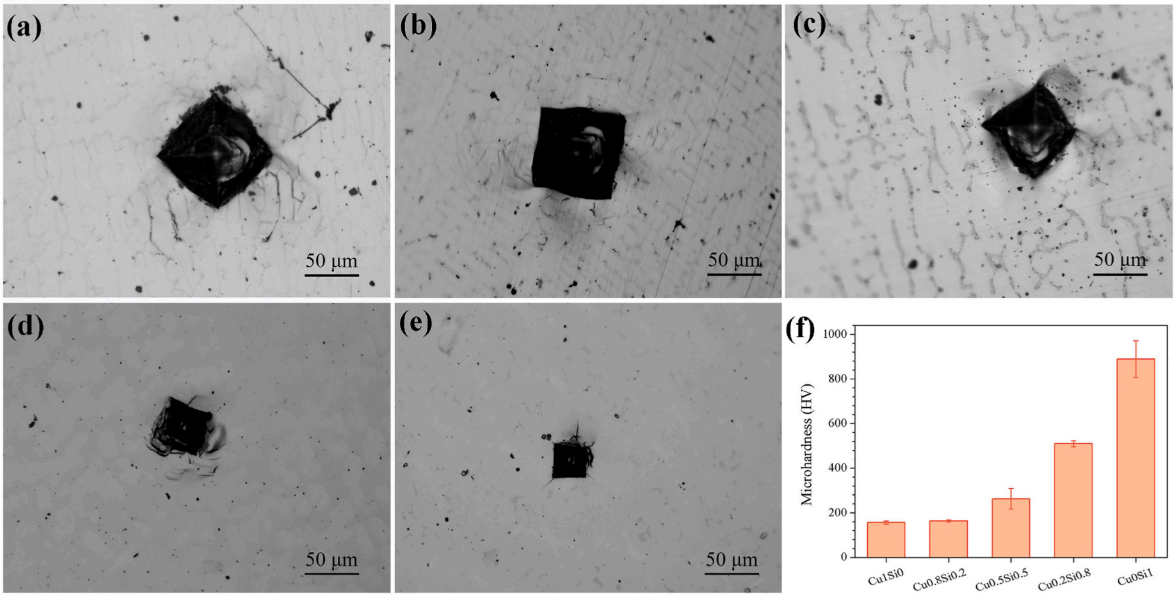

Fig. 6. The Vickers' indentation images (a–e) and microhardness (f) of CoCrFeNiCu$_{1\text{-}x}$Si$_x$ alloys. (a) Cu$_1$Si$_0$ alloy; (b) Cu$_{0.8}$Si$_{0.2}$ alloy; (c) Cu$_{0.5}$Si$_{0.5}$ alloy; (d) Cu$_{0.2}$Si$_{0.8}$ alloy; (e) Cu$_0$Si$_1$ alloy.

promoted the transformation from soft FCC phase to hard BCC phase, increasing the microhardness of CoCrFeNiCu$_{1-x}$Si$_x$ alloys.

Fig. 7(a) shows the typical load-displacement curves of CoCrFeNiCu$_{1-x}$Si$_x$ alloys. All tested alloys exhibited a smooth and continuous deformation behavior. Fig. 7(b) indicates that the *H* value of CoCrFeNiCu$_{1-x}$Si$_x$ alloys increased in general as the *x* value increased, which is almost consistent with the microhardness shown in Fig. 6(f). Sun et al. [39] has reported that the Young's modulus was proportional to the hardness of all materials. Nonetheless, Fig. 7(b) indicates that Cu$_{0.8}$Si$_{0.2}$ alloy exhibited a lower *E* value than Cu$_1$Si$_0$ alloy, which might be attributed to the increasing fraction of soft FCC phase. As the *x* value further increased, the *E* value of CoCrFeNiCu$_{1-x}$Si$_x$ alloys showed a similar trend to the *H* value, which was attributed to the formation of hard BCC and NiSi-rich phases. It has been reported that the H/E and H^3/E^2 ratios were considered as mechanical parameters useful for predicting the plastic deformation resistance and wear resistance of materials [40]. In Fig. 7(c), the H/E and H^3/E^2 ratios of CoCrFeNiCu$_{1-x}$Si$_x$ alloys increased with the increasing *x* value, suggesting the improved wear resistance [41]. Fig. 7(d) shows the fracture toughness (K_{IC}) of CoCrFeNiCu$_{1-x}$Si$_x$ alloys calculated by the energy-based method. When the *x* value increased from 0 to 0.5, the K_{IC} value firstly decreased from 9.26 MPa·m$^{1/2}$ (Cu$_1$Si$_0$ alloy) to 7.34 MPa·m$^{1/2}$ (Cu$_{0.8}$Si$_{0.2}$ alloy) and then increased to 8.65 MPa·m$^{1/2}$ (Cu$_{0.5}$Si$_{0.5}$ alloy). This was related to the microstructure change of CoCrFeNiCu$_{1-x}$Si$_x$ alloys. This was related to the microstructure change of CoCrFeNiCu$_{1-x}$Si$_x$ alloys. It has been reported that the FCC structure usually possessed a large amount of slip systems that moved easily and thus sufficient plastic deformation could occur at the crack trip through a dislocation-mediated plasticity, resulting in the high fracture toughness [42]. Therefore, the increasing content of FCC phase in CoCrFeNiCu$_{1-x}$Si$_x$ alloys would enhance the fracture toughness. However, its relatively increasing grain size also led to the appearance of extra holes near the crack tip or at grain boundaries and thus reduced the required energy for the initiation or propagation of cracks, resulting in a decrease in the fracture toughness [43]. The competitive effect between them led to the variation in the K_{IC} value of CoCrFeNiCu$_{1-x}$Si$_x$ alloys ($0 \le x \le 0.5$). As the *x* value further increased to 1, the soft FCC phase gradually transformed into the brittle BCC phase that could not adapt to accommodate the sufficient plastic deformation a the crack tip due to the lack of slip systems that required lower stress to activate the movement. The increasing grain size of the BCC phase also caused the reduced fracture toughness. Meanwhile, the formation of the brittle NiSi-rich phase could cause the high stress concentration and promoted the initiation of cracks. Therefore, the K_{IC} value decreased to 8.57 MPa·m$^{1/2}$ for Cu$_{0.2}$Si$_{0.8}$ alloy and 7.56 MPa·m$^{1/2}$ for Cu$_0$Si$_1$ alloy.

3.5. Tribological properties

Fig. 8(a) shows the coefficient friction (COF) curves of CoCrFeNiCu$_{1-x}$Si$_x$ alloys after dry sliding at 2 N. It can be seen that the wear process of CoCrFeNiCu$_{1-x}$Si$_x$ alloys can be divided into the initial running-in stage and the stable wear stage. The average COF in Fig. 8(b) indicates that the average COF decreased from 0.679 to 0.246 as the *x* value in CoCrFeNiCu$_{1-x}$Si$_x$ alloys increased from 0 to 1. This trend is negatively correlated with the change in hardness, which is consistent with results obtained by other studies [44,45].

Fig. 9(a) shows the typical wear track profiles of CoCrFeNiCu$_{1-x}$Si$_x$ alloys after dry sliding at 2 N. It can be seen that the depth and width of the wear track decreased as the *x* value increased, suggesting a reduced wear loss. To further quantify the influence of Cu and Si on wear resistance, the wear rate (*W*) of CoCrFeNiCu$_{1-x}$Si$_x$ alloys was calculated and shown in Fig. 9(b). It can be seen that the *W* value decreased from 4.84×10^{-4} to 0.76×10^{-4} mm^3·N^{-1}·m^{-1} as the *x* value in CoCrFeNiCu$_{1-x}$Si$_x$ alloys increased from 0 to 1. Therefore, the decreasing Cu content and increasing Si content could lead to a great improvement in the wear resistance of CoCrFeNiCu$_{1-x}$Si$_x$ alloys, which is related to the change in the phase composition and microstructure. A comparison of

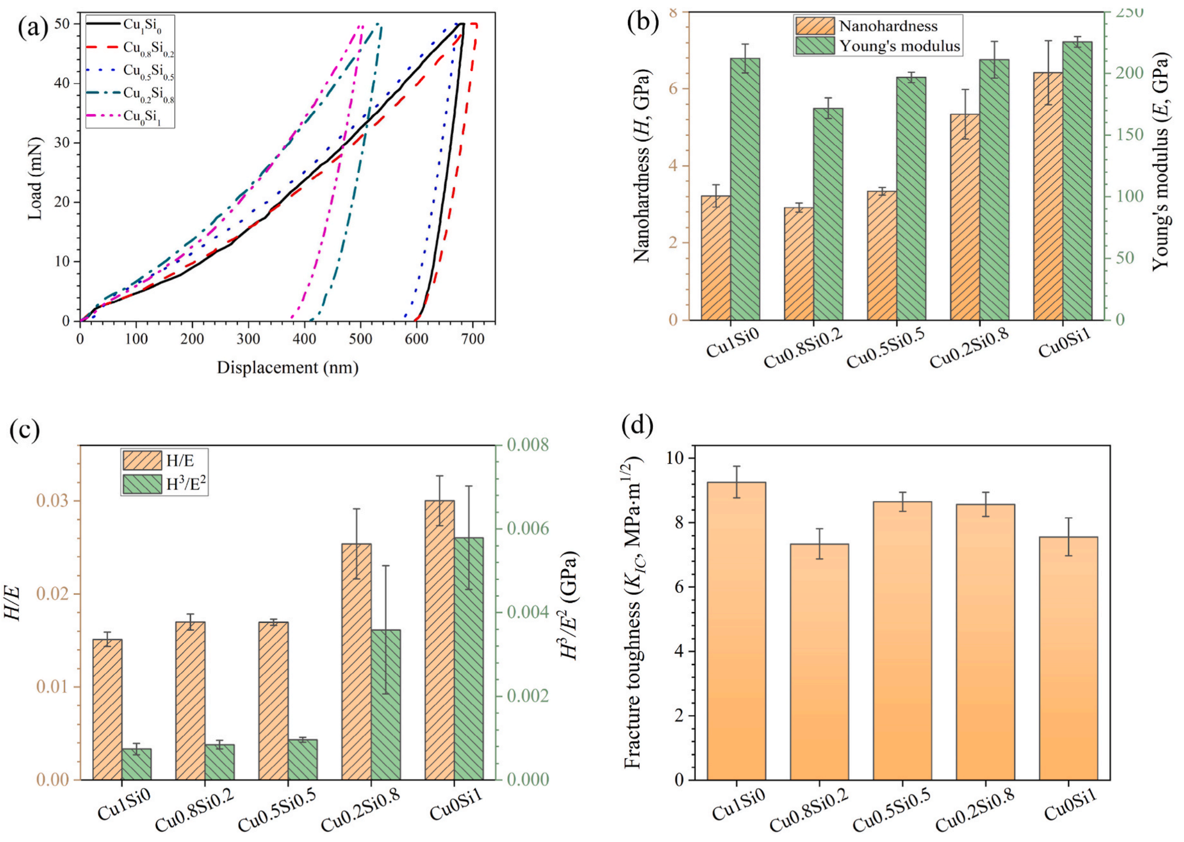

Fig. 7. Load-displacement curves (a), nanohardness and Young's modulus (b), H/E, H^3/E^2 (c) and fracture toughness (d) of CoCrFeNiCu$_{1-x}$Si$_x$ alloys.

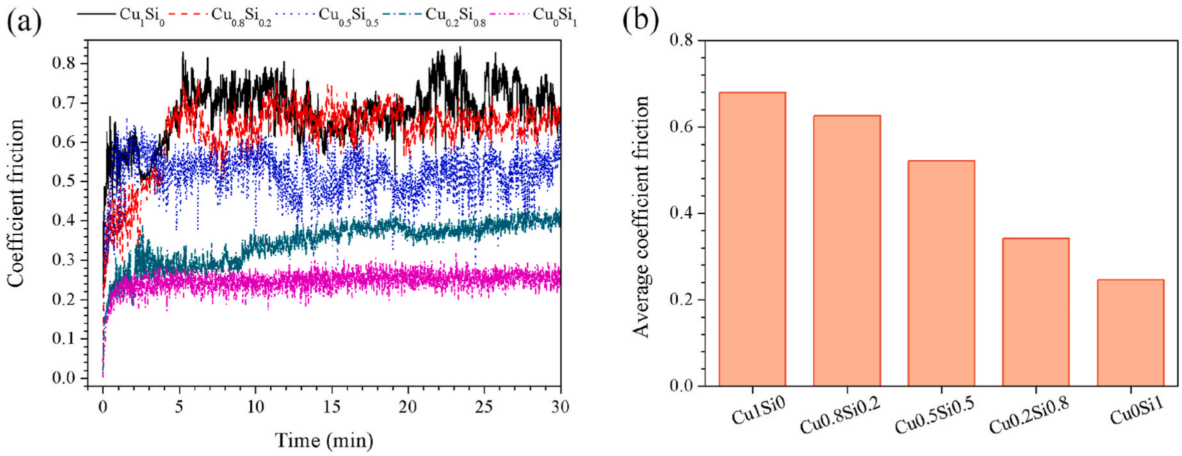

Fig. 8. The coefficient friction (COF) curves (a) and average COF (b) of CoCrFeNiCu$_{1\text{-}x}$Si$_x$ alloys after dry sliding at 2 N.

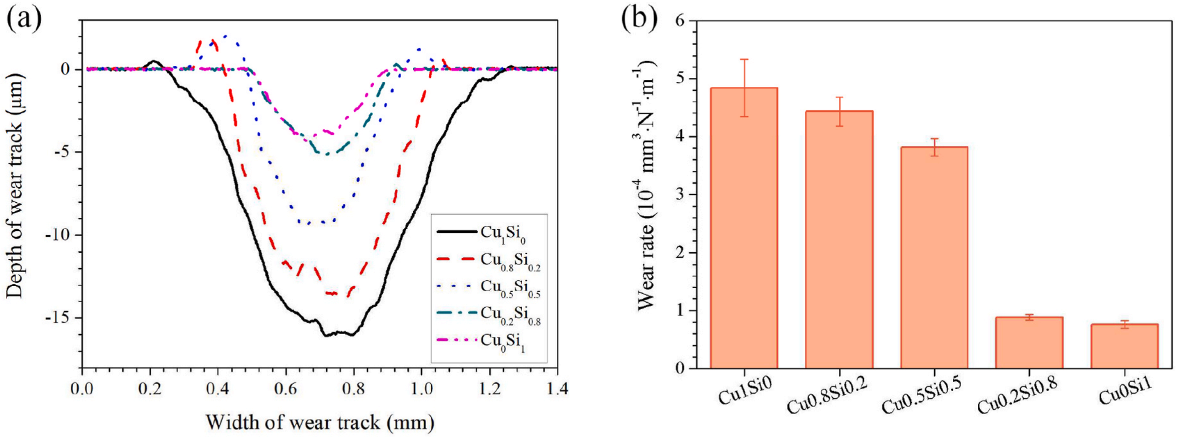

Fig. 9. The typical wear track profiles (a) and wear rate (b) of CoCrFeNiCu$_{1\text{-}x}$Si$_x$ alloys after dry sliding at 2 N.

microhardness vs. wear rate between this study and other HEAs systems [20,46–57] is shown in Fig. 10. It can be seen that both Cu$_{0.2}$Si$_{0.8}$ and Cu$_0$Si$_1$ alloys in this study exhibited a fair balance between the high hardness and low wear rate, compared with other CoCrFeNi-X, FeCrNSi$_x$, CrFeNiNb$_x$, Al$_x$CoCrFeNi$_y$, NbMoZrTi-X HEAs systems. Therefore, both Cu$_{0.2}$Si$_{0.8}$ and Cu$_0$Si$_1$ alloys could display a particularly promising applications in aerospace, automotive, energy, etc.

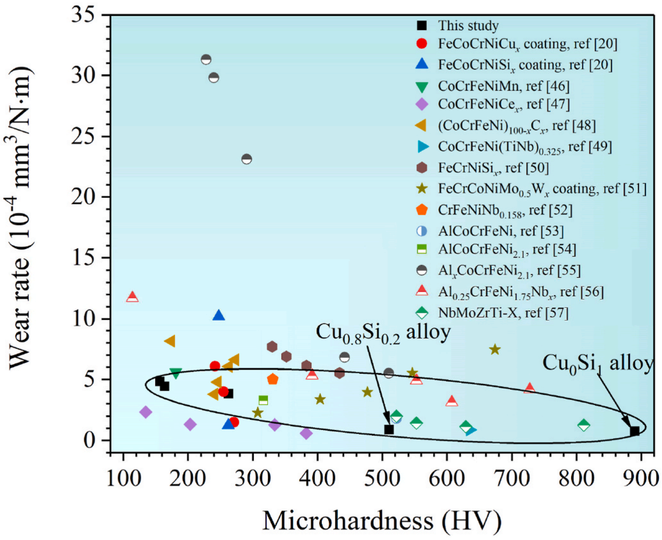

Fig. 10. A comparison of microhardness vs. wear rate between this study and other HEAs systems.

Fig. 11 shows the morphologies of the worn surfaces for CoCrFeNiCu$_{1\text{-}x}$Si$_x$ alloys. Fig. 11(a and b) indicates that the worn surface of the Cu$_1$Si$_0$ alloy exhibited obvious plastic deformation and a large amount of patches. The corresponding EDS mapping results of the worn surfaces in Fig. 12(a) indicate that the presence of oxygen element in the patches, suggesting the formation of oxide patches during the dry sliding. This was due to the surface oxidation reaction caused by the generation of heat during the friction process. These characteristics indicates that the Cu$_1$Si$_0$ alloy experienced an adhesive wear. Meanwhile, there are many wear debris and plowing grooves were formed due to its low hardness, suggesting the presence of the abrasive wear. Therefore, the main wear mechanism of the Cu$_1$Si$_0$ alloy was adhesive wear and abrasive wear. For Cu$_{0.8}$Si$_{0.2}$ and Cu$_{0.5}$Si$_{0.5}$ alloys, Fig. 11(c–f) and Fig. 12(b and c) show that the plastic deformation disappeared from the worn surface, while the oxide patches could be still detected but their content was relatively lower. Moreover, the amount of wear debris increased and the plowing grooves could still be observed. Accordingly, the main wear mechanism of Cu$_{0.8}$Si$_{0.2}$ and Cu$_{0.5}$Si$_{0.5}$ alloys was the abrasive wear. For Cu$_{0.2}$Si$_{0.8}$ and Cu$_0$Si$_1$ alloys, Fig. 11(g–j) and Fig. 12(d and e) show that the oxide patches could not be detected, and the worn surface did not exhibit distinct plowing grooves and became relatively smoother, suggesting that the matrix experienced the slight abrasive wear. In summary, when the x value of CoCrFeNiCu$_{1\text{-}x}$Si$_x$ alloys increased from 0 to 1, the main wear mechanism changed from adhesive wear and abrasive wear to

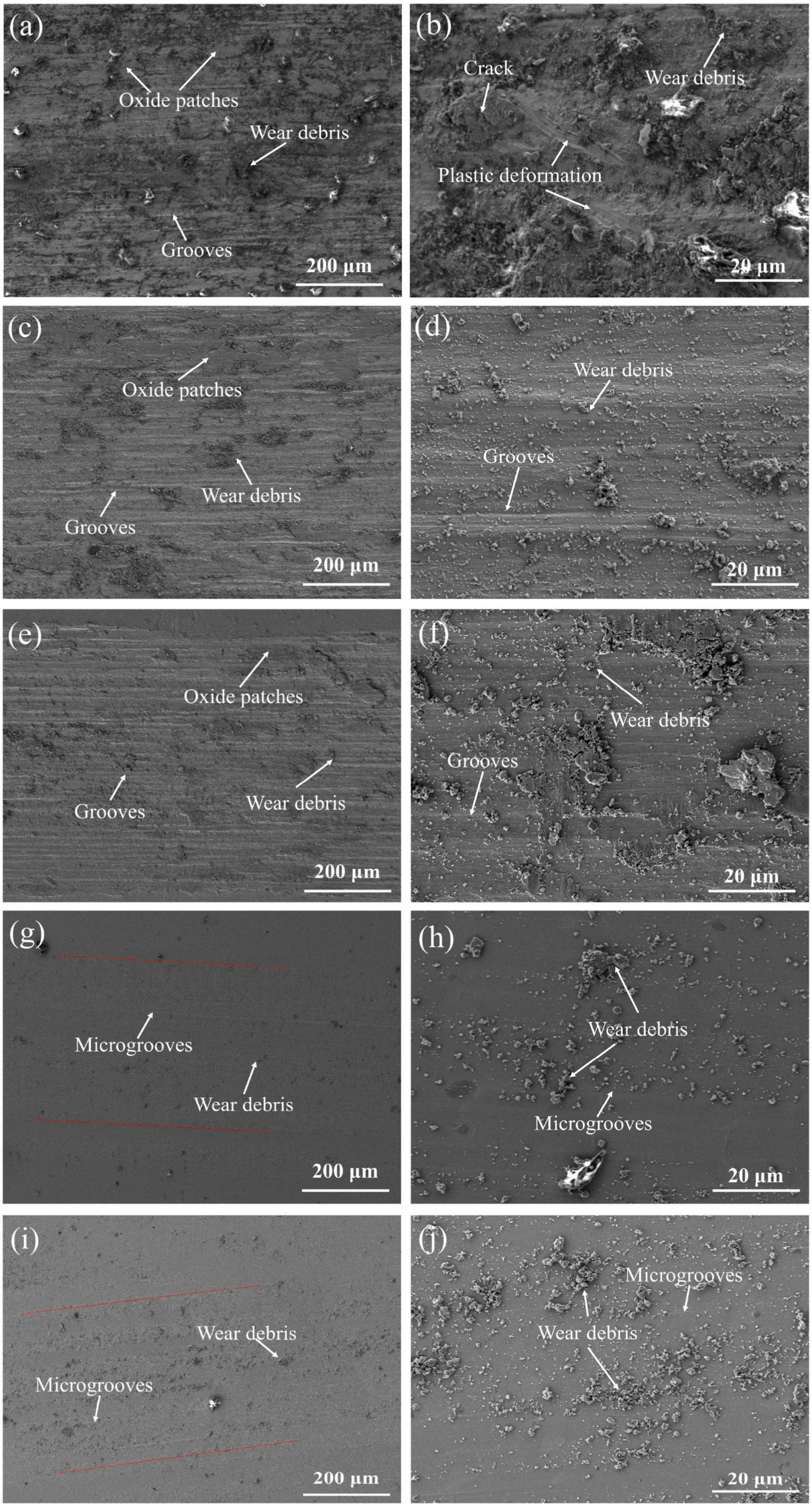

Fig. 11. The morphologies of the worn surfaces for CoCrFeNiCu$_{1-x}$Si$_x$ alloys after dry sliding at 2 N (a, b) Cu$_1$Si$_0$ alloy; (c, d) Cu$_{0.8}$Si$_{0.2}$ alloy; (e, f) Cu$_{0.5}$Si$_{0.5}$ alloy; (g, h) Cu$_{0.2}$Si$_{0.8}$ alloy; (i, j) Cu$_0$Si$_1$ alloy.

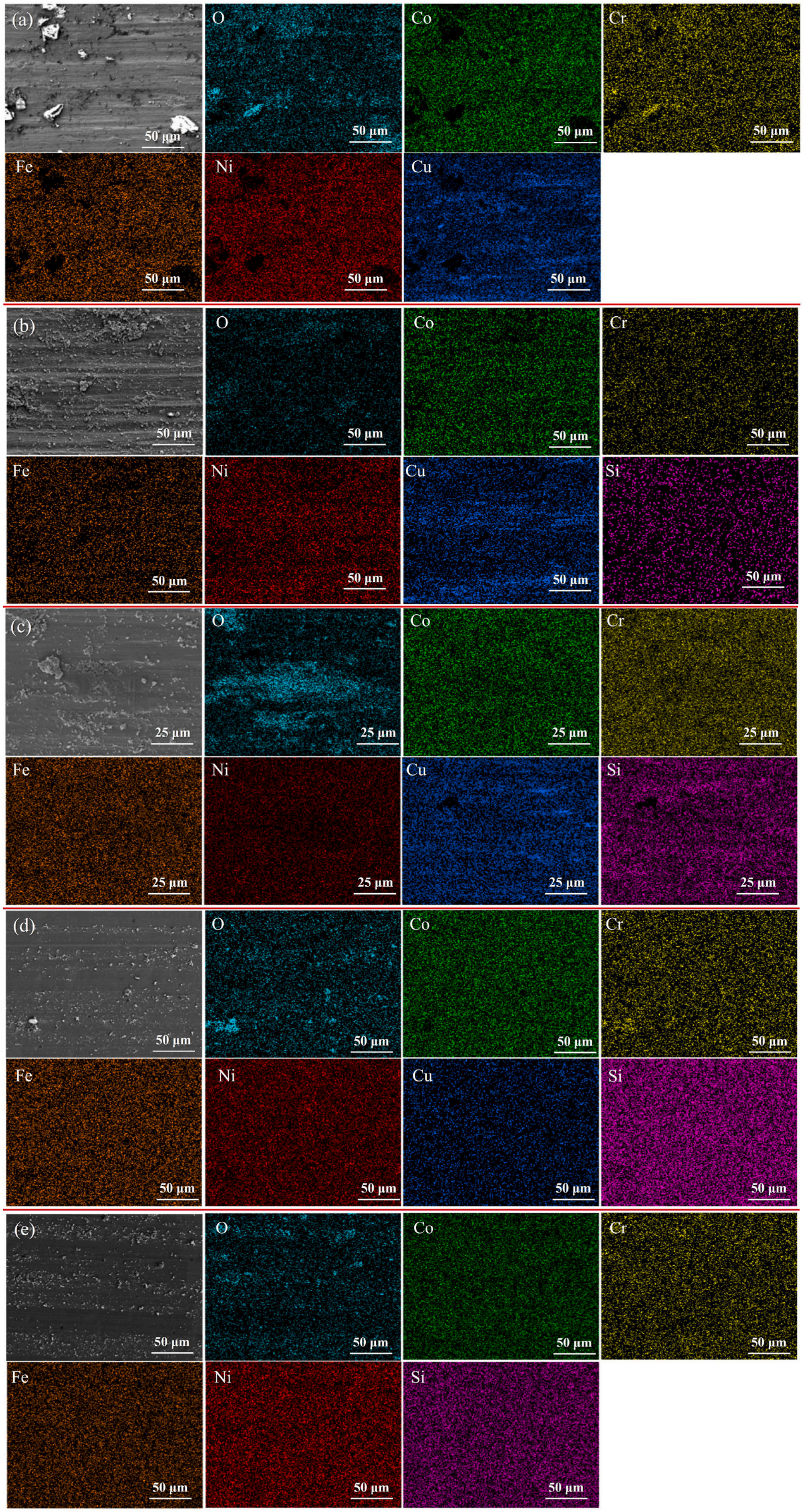

Fig. 12. The EDS mapping results of the worn surfaces for CoCrFeNiCu$_{1\text{-}x}$Si$_x$ alloys after dry sliding at 2 N (a) Cu$_1$Si$_0$ alloy; (b) Cu$_{0.8}$Si$_{0.2}$ alloy; (c) Cu$_{0.5}$Si$_{0.5}$ alloy; (d) Cu$_{0.2}$Si$_{0.8}$ alloy; (e) Cu$_0$Si$_1$ alloy.

slight abrasive wear. This might be related to the increasing hardness caused by the decreasing Cu content and increasing Si content in CoCrFeNiCu$_{1\text{-}x}$Si$_x$ alloys.

Fig. 13 shows the XPS spectra of Co, Cr, Fe, Ni, Cu and Si elements on the worn surface for CoCrFeNiCu$_{1\text{-}x}$Si$_x$ alloys after dry sliding at 2 N. The Co2p spectra could be divided to peaks at 777.7 ± 0.3 and 792.5 ± 0.3 eV for metallic Co, peaks at 780.7 ± 0.2 and 796.4 ± 0.2 eV for CoO and corresponding satellite peaks at 785.4 ± 0.3 and 801.7 ± 0.2 eV [58]. In the Cr2p spectra, peaks at 573.5 ± 0.2 and 582.9 ± 0.2 eV could be associated with metallic Cr, while those at 576.5 ± 0.1 and 586.1 ± 0.4 eV were corresponding to Cr_2O_3 [59]. The Fe2p spectra could decompose into peaks at 706.6 ± 0.3 eV and 719.4 ± 0.3 eV for metallic Fe, peaks at 710.2 ± 0.3 eV and 722.9 ± 0.3 eV for FeO and peaks at 712.4 ± 0.3 eV and 726.2 ± 0.3 eV for Fe_2O_3, respectively [60]. The Ni2p spectra could decompose into peaks at 852.2 ± 0.2 and 869.4 ± 0.3 eV for metallic Ni, peaks at 854.9 ± 0.5 and 873.0 ± 0.2 eV for NiO and corresponding satellite peaks at 861.1 ± 0.2 and 878.6 ± 0.5 eV, respectively [61]. In Cu2p spectra, peaks at 932.0 ± 0.3 and 951.7 ± 0.2 eV could be associated with metallic Cu, while those at 934.4 ± 0.4 and 954.4 ± 0.7 eV were assigned to CuO [62]. The Si 2p spectra could decompose into peaks at 99.1 ± 0.3 and 101.5 ± 0.2 eV for metallic Si and SiO_2, respectively [63]. These results indicate that dry sliding friction experiment could lead to the oxidation of Co, Cr, Fe, Ni, Cu and Si elements that formed an oxide friction layer with excellent wear resistance.

Fig. 14(a) shows the atomic ratio of Co, Cr, Fe, Ni, Cu and Si elements on the worn surface of CoCrFeNiCu$_{1\text{-}x}$Si$_x$ alloys after dry sliding at 2 N. It can be seen that the atomic ratio of each Co, Cr, Fe and Ni on the worn surface of five alloys was mostly smaller than that in matrix. Meanwhile, the atomic ratio of Cu decreased from 24.5 % to 0, whereas that of Si

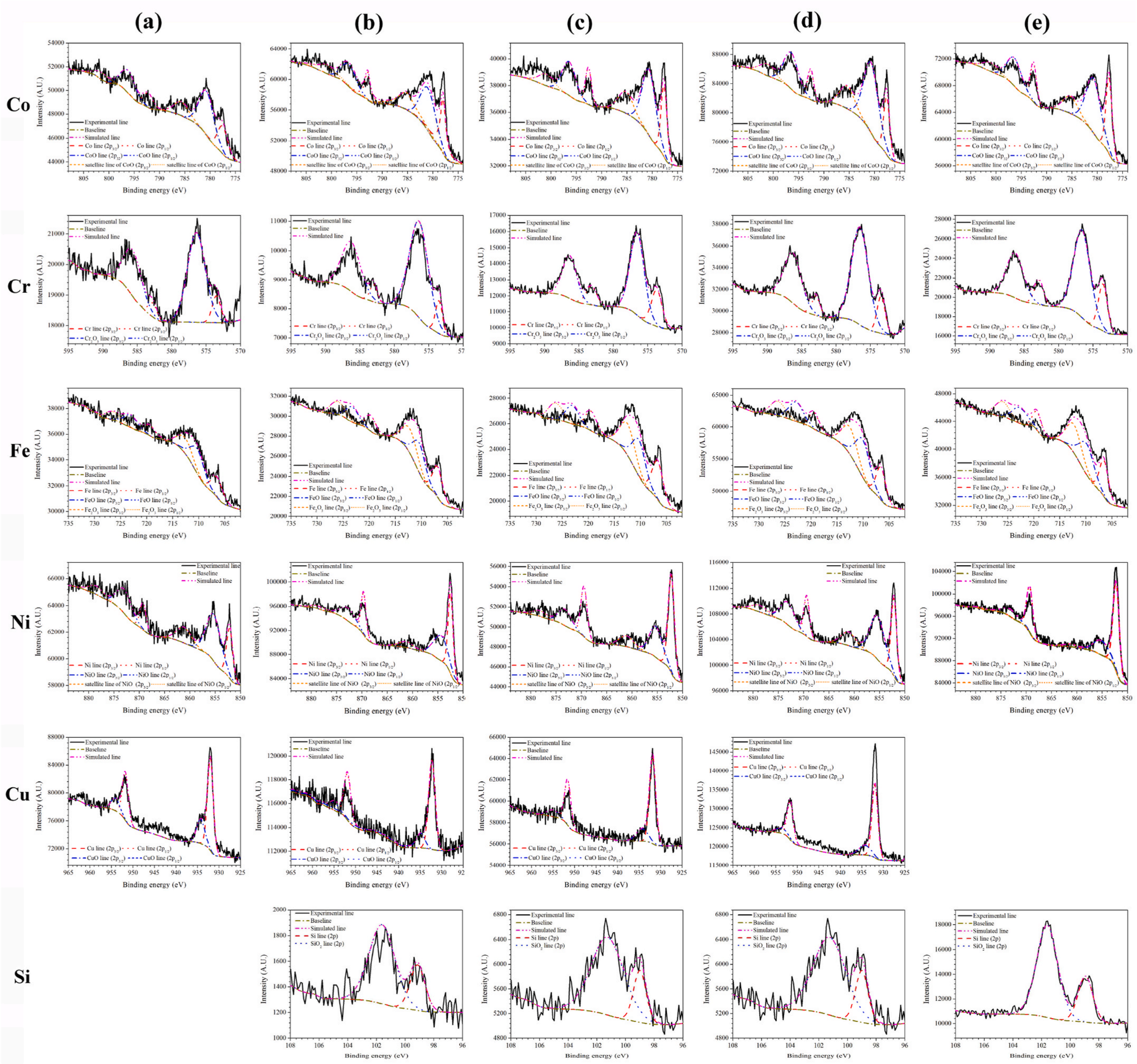

Fig. 13. XPS spectra of Co, Cr, Fe, Ni, Cu and Si elements on the worn surface for CoCrFeNiCu$_{1\text{-}x}$Si$_x$ alloys after dry sliding at 2 N (a) Cu$_1$Si$_0$ alloy; (b) Cu$_{0.8}$Si$_{0.2}$ alloy; (c) Cu$_{0.5}$Si$_{0.5}$ alloy; (d) Cu$_{0.2}$Si$_{0.8}$ alloy; (e) Cu$_0$Si$_1$ alloy.

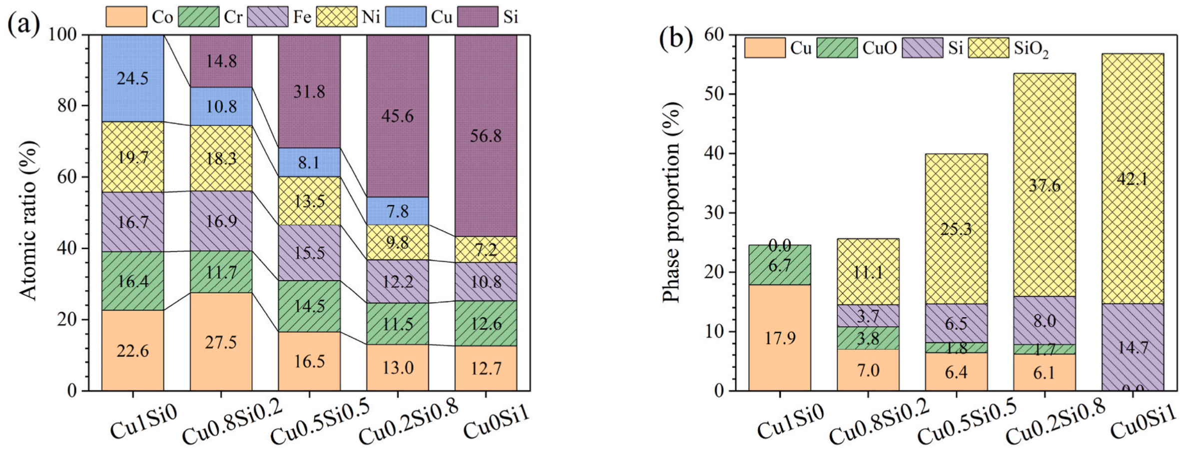

Fig. 14. Atomic ratio of Co, Cr, Fe, Ni, Cu and Si elements (a), phase proportion of the compounds of Cu and Si (b) on the worn surface of CoCrFeNiCu$_{1\text{-}x}$Si$_x$ alloys after dry sliding at 2 N.

increased from 0 to 56.8 % as the x value increased from 0 to 1. Therefore, the compounds of Cu and Si played an important role during dry sliding. Fig. 14(b) shows the phase proportion of the compounds of Cu and Si on the worn surface. It can be seen that Cu element mainly existed in the form of metallic Cu instead of CuO that could act as lubricants. Meanwhile, Si element mainly formed hard SiO$_2$ that could act as lubricants. Moreover, Cu content decreased, while SiO$_2$ content increased as the x value increased, resulting in the improved wear resistance and reduced COF.

In summary, the improved wear resistance of CoCrFeNiCu$_{1\text{-}x}$Si$_x$ alloys caused by the increasing x value could be attributed to the change in the microstructure and chemical composition with. From the microstructure, the decreasing Cu content and increasing Si content in CoCrFeNiCu$_{1\text{-}x}$Si$_x$ alloys brought about a change in phase composition and grain size, thus increasing the hardness as discussed in Section 3.4. It is well known that materials with a low hardness were less capable of withstanding the pressure of the hard counterpart, and thus led to a large contact area between them. During sliding, the shear forces caused by the relative motion of the counterpart produced a large amount of wear debris and deep grooves and thus roughened the surface, resulting in a high COF and wear loss. The increasing hardness of CoCrFeNiCu$_{1\text{-}x}$Si$_x$ alloys produced a higher resistance against the relative motion of the GCr15 steel ball and reduced the contact area between them. Therefore, both the width and depth of wear track as shown in Fig. 9(a) showed a continuously decreasing trend, contributing to the decrease in the COF and wear rate. Meanwhile, the increasing x value also led to the decreasing Cu content mainly in form of metallic Cu and increasing Si content mainly in form of lubricant SiO$_2$ on the worn surface of CoCrFeNiCu$_{1\text{-}x}$Si$_x$ alloys, which is shown in Fig. 14. On the one hand, the beneficial effect of Cu on the CoCrFeNi HEA system was mainly due to the formation of copper oxide that avoided direct contact and reduced the wear loss. However, only about 30 % of Cu element was oxidized in this work and thus the decrease in Cu content might help in improving the wear resistance. On the other hand, the formation of lubricant SiO$_2$ on the worn surface not only limited the direct contact between the counterpart materials and alloy surface, but also had a lubricating effect during sliding. Accordingly, the increasing Si content could improve the wear resistance. Consequently, the change in the chemical composition with the increasing x value also brought about a decrease in the COF and wear rate.

4. Conclusion

(1) As the x value increased from 0 to 0.5, the microstructure of CoCrFeNiCu$_{1\text{-}x}$Si$_x$ alloys changed from FCC + Cu-rich to FCC + Cu-rich + NiSi-rich phases, suggesting that Si addition promoted the formation of intermetallic compounds. Moreover, as the x value increased, the grain size and area fraction of FCC phase increased. When the x value further increased to 1, the microstructure became FCC + BCC + NiSi-rich phases, suggesting the phase transition from FCC to BCC caused by Si addition.

(2) As the x value in CoCrFeNiCu$_{1\text{-}x}$Si$_x$ alloys increased from 0 to 1, the I_{corr} value decreased from 8.63×10^{-7} to 3.81×10^{-8} A/cm^2, whereas the R_{ct} value increased from 3.66×10^3 to 6.16×10^5 Ω·cm^2. Therefore, the corrosion resistance of CoCrFeNiCu$_{1\text{-}x}$Si$_x$ alloys was improved by the decrease in Cu content and increase in Si content. This was related to the competition among the decreasing content of Cu-rich phase that resulted in the serious galvanic corrosion, the increasing content of NiSi-rich phase that led to the formation of new galvanic couple deteriorating the corrosion resistance, and the increasing content of BCC phase that could prevent FCC phase from being corroded. Moreover, CoCrFeNiCu$_{1\text{-}x}$Si$_x$ alloys transformed into a spontaneous passivation process when the x value increased to 0.8.

(3) As the x value increased, the hardness of CoCrFeNiCu$_{1\text{-}x}$Si$_x$ alloys exhibited an overall increasing trend, while the fracture toughness showed an opposite trend. This was related to the change in the lattice constant, grain size and area fraction of soft FCC phase, the disappearance of Cu-rich phase and the formation of hard BCC and NiSi-rich phase, which was caused by the decreasing Cu content and increasing Si content.

(4) As the x value increased from 0 to 1, the W value of CoCrFeNiCu$_{1\text{-}x}$Si$_x$ alloys decreased from 4.84×10^{-4} to 0.76×10^{-4} mm^3·N^{-1} · m^{-1}, suggesting an improved wear resistance. This was related to the improved hardness, increasing content of lubricant SiO$_2$ and decreasing content of metallic Cu during wear process. Moreover, the main wear mechanism of CoCrFeNiCu$_{1\text{-}x}$Si$_x$ alloys changed from adhesive wear and abrasive wear to slight abrasive wear.

(5) Comparison of the properties among five CoCrFeNiCu$_{1\text{-}x}$Si$_x$ alloys shows that the Cu$_{0.2}$Si$_{0.8}$ alloy exhibited an excellent comprehensive properties, revealed by the I_{corr} value of 4.81×10^{-8} A/cm^2, the R_{ct} value of 4.98×10^5 Ω·cm^2, the H value of 510.5 HV, the K_{IC} value of 8.57 MPa·m$^{1/2}$ and the W value of 0.88 mm^3·N^{-1} · m^{-1}.

CRediT authorship contribution statement

Xuehui Hao: Writing – review & editing, Writing – original draft, Resources, Funding acquisition, Data curation, Conceptualization. **Shihao Fan:** Formal analysis. **Ping Lu:** Investigation. **Shuai Yao:** Methodology. **Yunhao Li:** Software. **Tianyan Lu:** Software. **Meijie Wang:** Methodology. **Jingru Chen:** Visualization. **Changzheng Wang:** Writing

– review & editing, Project administration.

Declaration of competing interest

Data availability

Data will be made available on request.

Acknowledgement

This work is supported by Shandong Province Natural Science Foundation of China (Grant Nos. ZR2020QE026) and Liaocheng University Students Innovation Plan (Grant Nos. CXCY2023008).

References

[1] B.X. Yu, Y.S. Ren, Y. Zeng, W.H. Ma, K. Morita, S. Zhan, Y. Lei, G.Q. Lv, S.Y. Li, J. Wu, Recent progress in high-entropy alloys: a focused review of preparation processes and properties, J. Mater. Res. Technol. 29 (2024) 2689–2719.

[2] S.K. Dewangan, C. Nagarjuna, R. Jain, R.L. Kumawat, V. Kumar, A. Sharma, B. Ahn, Review on applications of artificial neural networks to develop high entropy alloys: a state-of-the-art technique, Mater. Today Commun. 37 (2023) 107928.

[3] D. Kumar, Recent advances in tribology of high entropy alloys: a critical review, Prog. Mater. Sci. 136 (2023) 101106.

[4] P. Sharma, V.K. Dwivedi, S.P. Dwivedi, Development of high entropy alloys: a review, Mater. Today Commun. 43 (2021) 502–509.

[5] J.L. Zhou, Y.H. Cheng, Y.X. Wan, H. Chen, Y.F. Wang, J.Y. Yang, Strengthening by Ti, Nb, and Zr doping on microstructure, mechanical, tribological, and corrosion properties of CoCrFeNi high-entropy alloys, J. Alloys Compd. 984 (2024) 173819.

[6] Z. Wu, S. Wang, Y. Jia, W. Zhang, R. Chen, B. Cao, S. Yu, J. Wei, Review on the tensile properties and strengthening mechanisms of additive manufactured CoCrFeNi-based high-entropy alloys, Metals 14 (2024) 437.

[7] D.F. Xu, M.L. Wang, T.X. Li, X.S. Wei, Y.P. Lu, A critical review of the mechanical properties of CoCrNi-based medium-entropy alloys, Microstructures 2 (2022) 2022001.

[8] H.F. Lei, C. Chen, X.C. Ye, H.J. Kang, Z. Li, J.W. Fu, T.Y. Zhang, Z.J. Gao, B. Li, D. Fang, L. Wang, Synergistic effect of Nb and W alloying on the microstructure and mechanical properties of CoCrFeNi high entropy alloys, J. Mater. Res. Technol. 28 (2024) 3765–3774.

[9] X.H. Gu, H.J. Yan, Q.H. Zhang, X.Z. Meng, L.K. Wu, F.H. Cao, Microstructure characterization and corrosion behavior of Al$_x$(CoCrFeNi)$_{100-x}$ (x = 0, 5, 10, 15, 20) high entropy alloys in 0.5 M H$_2$SO$_4$ solution, J Alloy, Compd 944 (2023) 169247.

[10] X.H. Hao, J.M. Zhen, X.C. Zhao, J. Ma, H. Chen, S. Guo, C.G. Wang, C.Z. Wang, Effect of Sn addition on the tribological behaviors of CoCrFeNi high entropy alloys, J Alloy, Compd 909 (2022) 164657.

[11] X. Li, Z.T. Li, Z.G. Wu, S.J. Zhao, W.D. Zhang, H.B. Bei, Y.F. Gao, Strengthening in Al-, Mo- or Ti-doped CoCrFeNi high entropy alloys: a parallel comparison, J. Mater. Sci. Technol. 94 (2021) 264–274.

[12] L.J. Miao, Y. Cao, J.F. Liu, Y. Xu, L. Sun, S.G. Zhou, Effects of Cu on the high-entropy alloys of Cu$_x$CoCrFeNi: experiment and molecular dynamics simulations, Vacuum 227 (2024) 113369.

[13] Q. Wang, Q. Hu, H.L. Wang, L.C. Zeng, Investigations on the microstructures and tribological behaviors of as-cast CrFeCoNiCu$_x$ high entropy alloys, Intermetallics 157 (2023) 107886.

[14] C. Meng, Z.H. Song, X.W. Qiu, G.L. Wang, C. Wu, X. Ren, W.B. Zhuang, X.L. Wang, Effect of Cu content on microstructure and properties of CoCrFeNiCu$_x$ high-entropy alloy coatings prepared by induction cladding, J Alloy, Compd 934 (2023) 167896.

[15] C. Meng, Z.H. Song, G.L. Wang, W.B. Zhuang, C. Wu, X.L. Wang, Microstructure and properties of CoCrFeNiCu high-entropy alloy coating prepared by induction cladding, Mater. Lett. 314 (2022) 131896.

[16] P. Muangtong, A. Rodchanarowan, D. Chaysuwan, N. Chanlek, R. Goodall, The corrosion behaviour of CoCrFeNi-x (x = Cu, Al, Sn) high entropy alloy systems in chloride solution, Corrosion Sci. 172 (2020) 108740.

[17] Y.C. Cai, Y. Chen, Z. Luo, F. Gao, L. Li, Manufacturing of Cernicus medium-entropy alloy coating using laser cladding technology, Mater. Des. 133 (2017) 91–108.

[18] L. Huang, X.J. Wang, F.C. Jia, X.C. Zhao, B.X. Huang, J. Ma, C.Z. Wang, Effect of Si element on phase transformation and mechanical properties for FeCoCrNiSi$_x$ high entropy alloys, Mater. Lett. 282 (2021) 128809.

[19] X.Y. Gu, Y.X. Zhuang, D. Huang, Corrosion behaviors related to the microstructural evolutions of as-cast Al$_{0.3}$CoCrFeNi high entropy alloy with addition of Si and Ti elements, Intermetallics 147 (2022) 107600.

[20] Z.X. Zhu, X.B. Liu, Y.F. Liu, S.Y. Zhang, Y. Meng, H.B. Zhou, S.H. Zhang, Effects of Cu/Si on the microstructure and tribological properties of FeCoCrNi high entropy alloy coating by laser cladding, Wear 512–513 (2023) 204533.

[21] Y. Garip, Tailoring oxidation resistance of Fe$_2$CoCrNi$_{0.5}$ based high entropy alloys by addition of alloying elements (Si, Cu and Si-Cu co-added), J Alloy, Compd 920 (2022) 165951.

[22] J.W. Ying, Z.M. Xie, Z.J. Jiang, Z.A. Li, B.X. Chen, Microscale fracture and creep analysis of 3D porous graphene-based cementitious material by nanoindentation test and energy-based method, Construct. Build. Mater. 409 (2023) 133992.

[23] Z.T. Jiang, Y.G. Li, M.K. Lei, An inverse problem in estimating fracture toughness of TiAlN thin films by finite element method based on nanoindentation morphology, Vacuum 192 (2021) 110458.

[24] H.H. Jiang, Q.M. Gong, M. Peterlechner, S.V. Divinski, G. Wilde, Microstructure analysis of a CoCrFeNi high-entropy alloy after compressive deformation, Mater. Sci. Eng. 888 (2023) 145785.

[25] Q.W. Guo, H. Hou, Y. Pan, X.L. Pei, Z. Song, P.K. Liaw, Y.H. Zhao, Hardening-softening of Al$_{0.3}$CoCrFeNi high-entropy alloy under nanoindentation, Mater. Des. 231 (2023) 112050.

[26] P. Cheng, Y.H. Zhao, X.T. Xu, S. Wang, Y.Y. Sun, H. Hou, Microstructural evolution and mechanical properties of Al0.3CoCrFeNiSix high-entropy alloys containing coherent nanometer-scaled precipitates, Mater. Sci. Eng. 772 (2020) 138681.

[27] Q. Hu, H.L. Wang, L.H. Qian, L.C. Zeng, Q. Wang, X.W. Liu, Effects of Cu additions on microstructure and mechanical properties of as-cast CrFeCoNiCu$_x$ high-entropy alloy, T. Nonferr. Metal. Soc. 33 (2023) 1803–1813.

[28] X. Yang, Y. Zhang, Prediction of high-entropy stabilized solid-solution in multi-component alloys, Mater. Chem. Phys. 132 (2012) 233–238.

[29] S. Guo, C. Ng, J. Lu, C.T. Liu, Effect of valence electron concentration on stability of fcc or bcc phase in high entropy alloys, J. Appl. Phys. 109 (2011) 103505.

[30] Y.T. Yan, J.H. Lin, T. Liu, B.S. Liu, B. Wang, L. Qiao, J.C. Tu, J. Cao, J.L. Qi, Corrosion behavior of stainless steel-tungsten carbide joints brazed with AgCuX (X = In, Ti) alloys, Corrosion Sci. 200 (2022) 110231.

[31] C. Ji, A. Ma, J. Jiang, Mechanical properties and corrosion behavior of novel Al-Mg-Zn-Cu-Si lightweight high entropy alloys, J. Alloys Compd. 900 (2022) 163508.

[32] J. Jin, J.Z. Zhang, M.L. Hu, X. Li, Investigation of high potential corrosion protection with titanium carbonitride coating on 316L stainless steel bipolar plates, Corrosion Sci. 191 (2021) 109757.

[33] N. Li, H. Zhang, L.H. Wu, Z.K. Li, H.M. Fu, D.R. Ni, P. Xue, F.C. Liu, B.L. Xiao, Z. Y. Ma, Simultaneously increasing mechanical and corrosion properties in CoCrFeNiCu high entropy alloy via friction stir processing with an improved hemispherical convex tool, Mater. Char. 203 (2023) 113143.

[34] X.H. Hao, X.C. Zhao, H. Chen, B.X. Huang, J. Ma, C.Z. Wang, Y.S. Yang, Comparative study on corrosion behaviors of ferrite-pearlite steel with dual-phase steel in the simulated bottom plate environment of cargo oil tanks, J. Mater. Res. Technol. 12 (2021) 399–411.

[35] X.H. Hao, Q.X. Fan, Y.Y. Li, R.P. Miao, J. Ma, H. Chen, X.C. Zhao, C.Z. Wang, Structural, mechanical and corrosion behaviors of the homogeneous and gradient CrAlSiN coatings in 3.5% NaCl solution, J. Mater. Res. Technol. 15 (2021) 2781–2791.

[36] Y.W. Li, C.Y. Dong, X.L. Gu, J.J. Pan, R. Zhang, Z.X. Mu, M. Wen, K. Zhang, Exploring the potential for simultaneous enhancement of mechanical, wear and corrosion performance of the CrB$_2$ protective film actuated by soluting Si, Ceram. Int. 49 (2023) 35082–35093.

[37] H. Yang, X.S. Liu, A.X. Li, R. Li, S. Xu, M.D. Zhang, P.F. Yu, S.B. Yu, M.H. Jiang, C. Huo, G. Li, Effect of silicon addition on the corrosion resistance of Al$_{0.2}$CoCrFe$_{1.5}$Ni high-entropy alloy in saline solution, J Alloy, Compd 964 (2023) 171226.

[38] S. Kasimuthumaniyan, A.A. Reddy, N.M.A. Krishnan, N.N. Gosvami, Understanding the role of post-indentation recovery on the hardness of glasses: case of silica, borate, and borosilicate glasses, J. Non-Cryst. Solids 534 (2020) 119955.

[39] W.J. Sun, S. Kothari, C.C. Sun, The relationship among tensile strength, Young's modulus, and indentation hardness of pharmaceutical compacts, Powder Technol. 331 (2018) 1–6.

[40] R.P. Li, H. Chen, X.H. Hao, X.C. Zhao, B.X. Huang, Microstructure, mechanical properties and tribocorrosion characteristics of (Mo$_{1-x}$Cr$_x$)$_5$Si$_3$ alloys, Int. J Refract. Met. H. 115 (2023) 106291.

[41] D.H. Chung, X.D. Liu, Y. Yang, Fracture of sigma phase containing Co–Cr–Ni–Mo medium entropy alloys, J Alloy, Compd 846 (2020) 156189.

[42] Y.H. Jo, K.Y. Doh, D.G. Kim, K. Lee, D.W. Kim, H. Sung, S.S. Sohn, D. Lee, H.S. Kim, B.J. Lee, S. Lee, Cryogenic-temperature fracture toughness analysis of non-equi-atomic V$_{10}$Cr$_{10}$Fe$_{45}$Co$_{20}$Ni$_{15}$ high-entropy alloy, J Alloy, Compd 809 (2019) 151864.

[43] Y. Kang, J.G. Guo, X.L. Li, Y.Z. Yu, Theoretical study on the influence of grain size on the strength, toughness and plastic deformation mechanism of pre-cracked polycrystalline high entropy alloys, Mater. Today Commun. 39 (2024) 109081.

[44] B. Chen, X.M. Li, W.J. Chen, L. Shang, L.M. Jia, Microstructural evolution, mechanical and wear properties, and corrosion resistance of as-cast CrFeNbTiMox Refractory high entropy alloys, Intermetallics 155 (2023) 107829.

[45] Y.W. Sun, Z.Y. Wang, W.W. Wang, X.J. Zhao, K.J. Zhu, H.H. Li, Y.Y. Zhao, Z.K. Yin, Wear and corrosion resistance of Al$_{1.2}$CoCrFeNiSc$_x$ high entropy alloys with scandium addition, J. Mater. Res. Technol. 27 (2023) 8023–8036.

[46] Z.M. Guo, A.J. Zhang, J.S. Han, J.H. Meng, Microstructure, mechanical and tribological properties of CoCrFeNiMn high entropy alloy matrix composites with addition of Cr$_3$C$_2$, Tribol. Int. 151 (2020) 106436.

[47] J.G. Gao, W.W. Chang, M. Zhou, Z.K. Wang, Z.H. Yu, H.C. Qian, D.W. Guo, D. W. Zhang, Microstructure, wear resistance and antibacterial behaviors of novel CoCrFeNiCe$_X$ high entropy alloys, J. Mater. Res. Technol. 31 (2024) 2180–2192.

[48] Z.L. Zhang, Y.F. Ling, J. Hui, F. Yang, X.H. Zhang, S.Y. Tan, Z.H. Xie, F. Fang, Effect of C additions to the microstructure and wear behaviour of CoCrFeNi high-entropy alloy, Wear 530–531 (2023) 205032.

[49] Y.L. Deng, Y.Y. Huang, Z.X. Xu, X.H. Wang, D. Dong, D.D. Zhu, T.F. Ma, Effects of annealing on the mechanical and wear resistance properties of a designed novel eutectic high-entropy alloy, J. Alloys Compd. 980 (2024) 173642.

[50] W.Z. Zhao, Y.L. Zhu, H. He, Z.H. Xie, F.Y. Wang, A. Fu, Effect of Si addition on the microstructure and tribological properties of FeCrNi medium entropy alloy, J. Mater. Res. Technol. 30 (2024) 1450–1457.

[51] X.A. Duan, S.R. Wang, G.Q. Wang, S.P. Gao, L.H. Wang, X.F. Yang, Microstructure evolution and frictional wear behavior of laser cladding $FeCrCoNiMo_{0.5}W_X$ high-entropy alloy coatings, Intermetallics 158 (2023) 107888.

[52] D.S. Liang, C.X. Wei, Z.Y. Li, Q.M. Zhuang, L. Yang, C. Wu, F.Z. Ren, Sliding wear behavior of a Laves phase-strengthened $CrFeNiNb_{0.158}$ alloy at room and elevated temperatures, Wear 554–555 (2024) 205469.

[53] Y.X. Wang, Y.J. Yang, H.J. Yang, M. Zhang, S.G. Ma, J.W. Qiao, Microstructure and wear properties of nitrided AlCoCrFeNi high-entropy alloy, Mater. Chem. Phys. 210 (2018) 233–239.

[54] J.W. Miao, H. Liang, A.J. Zhang, J.Y. He, J.H. Meng, Y.P. Lu, Tribological behavior of an $AlCoCrFeNi_{2.1}$ eutectic high entropy alloy sliding against different counterfaces, Tribol. Int. 153 (2021) 106599.

[55] Y. Gan, S.G. Duan, Y.M. Mo, Y. Dong, J.L. Yi, Y.J. Hu, Effects of Al addition on the microstructure and mechanical properties of $Al_XCoCrFeNi_{2.1}$ high-entropy alloys, Intermetallics 166 (2024) 108172.

[56] Q.L. Li, S.Y. Lv, X.W. Hu, Y.F. Lan, J.Z. Liu, Effects of Nb additions on the microstructure and tribological properties of $Al_{0.25}CrFeNi_{1.75}$ high-entropy alloy, Intermetallics 151 (2022) 107715.

[57] W.J. Chen, X.M. Li, Microstructure, wear and corrosion resistance mechanism of as-cast lightweight refractory NbMoZrTiX (X = al, V) high-entropy alloys, J. Mater. Res. Technol. 31 (2024) 1215–1228.

[58] Y.L. Xie, A. Miche, V. Vivier, M. Turmine, Electrodeposition of Ni-Co alloys from neat protic ionic liquid: application to the hydrogen evolution reaction, Appl. Surf. Sci. 635 (2023) 157693.

[59] S.K. Dewangan, S. Kumar, O. Maulik, G.M. Pillai, V. Kumar, B. Ahn, XPS study on passivation behavior of naturally formed oxide on $AlFeCuCrMg_{1.5}$ high-entropy alloy, Chem. Phys. Lett. 841 (2024) 141171.

[60] T.Y. Cui, H.C. Qian, W.W. Chang, H.B. Zheng, D.W. Guo, C.T. Kwok, L. Mou Tam, D.W. Zhang, Towards understanding *Shewanella algae*-induced degradation of passive film of stainless steel based on electrochemical, XPS and multi-mode AFM analyses, Corrosion Sci. 218 (2023) 111174.

[61] N. Ribière, J. Esvan, N. Engler, D. Brimbal, M. Skocic, É. Andrieu, C. Blanc, L. Laffont, An XPS and TEM study of the composition and structure of native oxides on the inner surface of as-received Ni base alloy steam generator tubes, Appl. Surf. Sci. 654 (2024) 159514.

[62] J.M. Wang, H. Jiang, X.X. Chang, L.J. Zhang, H.X. Wang, L. Zhu, S.X. Qin, Effect of Cu content on the microstructure and corrosion resistance of $AlCrFeNi_3Cu_x$ high entropy alloys, Corrosion Sci. 221 (2023) 111313.

[63] Y.Y. Liu, Z.P. Yao, P. Zhang, Z. Xu, S.Y. Lin, M.Y. He, S.T. Lu, X.H. Wu, Tailoring high-temperature oxidation resistance of $FeCrMnVSi_x$ high entropy alloy coatings via building Si-rich dendrite microstructure, Appl. Surf. Sci. 606 (2022) 154862.